Developments in the Built Environment 17 (2024) 100326

Contents lists available at ScienceDirect

Developments in the Built Environment

journal homepage: www.sciencedirect.com/journal/developments-in-the-built-environment

Incorporating façade-specific climatic factors to improve the ISO 15927-3 characterisation of wind-driven rain spells: Dutch and Spanish case studies

José M. Pérez-Bella [a,*], Javier Domínguez-Hernández [a], Elena Ibarz-Montaner [b], Martín Orna-Carmona [c], Ángel Salesa-Bordanaba [c], Scott A. Orr [d]

[a] Department of Construction Engineering, Engineering and Architecture School, University of Zaragoza, María de Luna, s/n, 50018 Zaragoza, Spain
[b] Department of Continuous Media Mechanics and Theory of Structures, Engineering and Architecture School, University of Zaragoza, María de Luna, s/n, 50018 Zaragoza, Spain
[c] La Almunia Polytechnic University School, University of Zaragoza, c/ Mayor, 5, 50100 La Almunia de Doña Godina, Spain
[d] Institute for Sustainable Heritage, The Bartlett Faculty of the Built Environment, University College London, 14 Upper Woburn Place, WC1H 0NN London, United Kingdom

ARTICLE INFO

Keywords:
Wind-driven rain
Façade design
ISO standard
Method reliability
Potential evaporation

ABSTRACT

ISO standard 15927-3 characterise episodic exposures of wind-driven rain (WDR) on building façades by identifying wetting intervals, referred to as spells. Spells separated by 96 h or more without WDR are considered, assuming that this interval is sufficient for evaporative losses to exceed prior rainwater gains. This approach ignores variations in evaporation due to the façade orientation and local environmental factors, which cause diverse drying intervals even for the same material. This study proposes an estimation of potential evaporation losses in façades, considering their orientation and local climate. Representative drying intervals and enhanced façade-specific WDR spells are identified by combining potential evaporation losses with the directional WDR exposure. The results at locations in The Netherlands and Spain demonstrates that the drying intervals can vary significantly depending on these factors (regardless of the surface materials), which suggests reconsidering the current 96-h ISO model to minimise uncertainties when characterising episodic WDR exposures.

1. Introduction

Precipitation deflected by wind action, referred to as wind-driven rain (WDR) constitutes the main source of water penetration for building façades and causes multiple issues concerning the deterioration of construction materials, performance of the building thermal envelope, and health within the indoor environment (Hall and Hoff, 2012; Abuku et al., 2009; Bastien and Winther-Gaasvig, 2018; Sauni et al., 2015). Therefore, being able to accurately determine exposure of building façades to WDR is a key task for defining suitable watertight designs.

ISO standard 15927-3 establishes a semi-empirical calculation for assessing WDR exposure on building façades, which evaluates a mean annual index as well as a spell index that represents exposure to WDR events associated with the most severe wetting period likely to occur in any given three-year period (each wetting period is known as 'spell'). Whereas the annual index describes the average rainwater supply on exposed façade materials, the spell index is related to temporary rainwater penetration, which usually requires an intense and transitory rainwater supply. Both WDR indices should be determined for several façade orientations by considering simultaneous hourly records of rainfall intensity and wind velocity (speed and direction) gathered for a minimum of ten years (EN ISO 15927-3, 2009). The alternative calculation established by the ISO standard for those sites without hourly climatic records is not considered in this study given its limited accuracy and methodological ambiguity (Pérez et al., 2020a).

These indices are commonly used as reference values to compare WDR exposure among different locations and regions, as well as to establish qualitative design guidelines for building façades through normative requirements. Specifically, the study of WDR spells is receiving increasing attention, both because of its impact on the WDR loads and water penetration of façades and their increasing relevance associated with climate change (Orr and Viles, 2018; Orr et al., 2018; Cornick and Lacasse, 2005). Each spell is defined in Annex B of ISO standard 15927-3 as a continued wetting period of no more than 96 h without WDR on the façade orientation (Fig. 1). This interval of 96 h represents the maximum time that may be required before evaporative

* Corresponding author. Department of Construction Engineering, University of Zaragoza (UZ) María de Luna, s/n, 50018, Zaragoza, Spain.
E-mail address: jmpb@unizar.es (J.M. Pérez-Bella).

https://doi.org/10.1016/j.dibe.2024.100326
Received 1 September 2023; Received in revised form 20 December 2023; Accepted 5 January 2024
Available online 14 January 2024

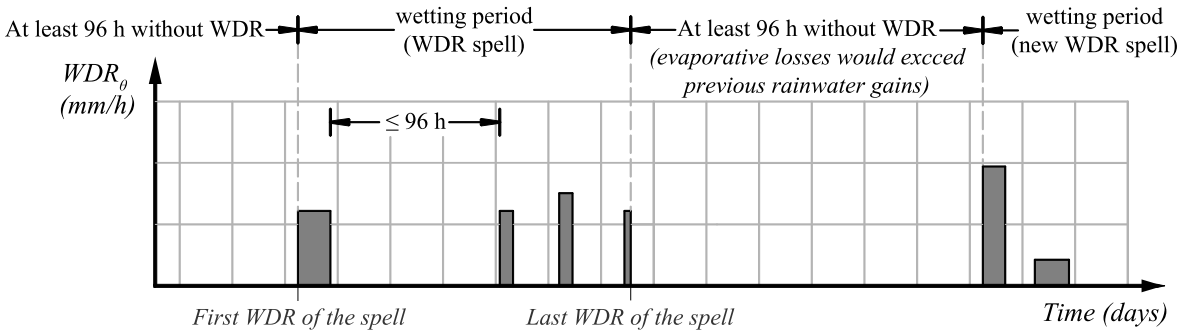

Fig. 1. Scheme of the WDR spell established by ISO standard 15927-3 (96-h ISO model). A separate analysis is required for each possible façade orientation θ.

losses exceed the previous water gains due to WDR. Because multiple spells separated by more than 96 h without WDR can occur throughout each year, the ISO standard only considers the WDR exposure (spell index) associated with the most severe spell likely to occur for each façade orientation in any given three-year period (EN ISO 15927-3, 2009).

It should be noted that this calculation of WDR exposure events assumes important simplifications in order to provide a fast and generic characterisation:

- Firstly, the 96-h ISO model omits the complex interaction between material properties and the evaporation process. Thus, part of the raindrops impinging on building façades can be lost by splashing or bounding, runoff along the façade or remain adhered, evaporate, or be absorbed by materials or infiltrated through the cladding (Blocken et al., 2013; Van Linden and Van Den Bossche, 2022). In turn, factors such as duration and intensity of WDR, previous wetting-drying history of the cladding and particular material properties determine the absorption, store and release of rainwater in porous materials (Hall and Hoff, 2012; Van Linden and Van Den Bossche, 2022; Beijer, 1977; Kahangi et al., 2021). When the façade surface nears saturation, WDR begins to runoff and detrimental infiltrations can occur into the enclosure (Van Linden and Van Den Bossche, 2022; Van Den Bossche et al., 2011). The discipline of building physics analyses these hygrothermal processes by means of heat-air-moisture simulations, which can be conducted by 1D, 2D, and 3D software such as WUFI and CHAMPS-BES, to mention just a couple (Fraunhofer Institute for Building Physics, 2023; Building Energy and Environmental Systems Laboratory, 2006). These models require exhaustive climatic records on a yearly basis (or prior data processing to obtain moisture reference years) and detailed knowledge of material properties and façade configuration (Zhou et al., 2016). Experimentally, absorption values between 76% and 92% of the applied water were reported on clay brick masonry during the first hours of wetting (Kahangi et al., 2021). In turn, various studies have identified rainwater infiltration rates ranging from 0.22% (mortared masonry brick walls) to 47.04% (glued masonry brick walls) for low pressure differences. Values between 0.5 and 2.0% have also been reported for wood frame walls, and approximately 0.50% of the WDR load can reach the air chamber in ventilated façades (Van Linden and Van Den Bossche, 2022; Van Den Bossche et al., 2011; Olsson, 2018; Arce et al., 2017).
Disregarding these approaches, the 96-h interval was generically established to bridge the gap between succeeding depressions in a weather sequence in the United Kingdom and based on some experimental findings on brick walls tested in the mid-20th century (Orr et al., 2018; Prior, 1985). The details of these old experimental works remain largely undefined (e.g. considered absorption-penetration rates, specific material properties of the samples, and criteria to determine that evaporative losses exceed the previous water gain). Consequently, the ISO standard should only be strictly applied to generically compare WDR exposures on brick wall designs in the United Kingdom. Despite this, the international standard is indiscriminately used to characterise spell indices anywhere and for any type of façade, although it should be assumed that 96 h is not a reliable interval to ensure that all previous rainwater gain has been evaporated.
- Secondly, the phenomenon of water evaporation also depends on multiple local factors including solar radiation, air temperature, relative humidity, and wind speed, which vary the evaporation interval required for each situation (Shuttleworth and Maidment, 1993; Shuttleworth, 2007). Some of these environmental factors, such as solar radiation, depend on the façade orientation considered; therefore, even for the same façade material, the evaporation intervals can vary depending on its location and orientation (Duffie and Beckman, 2013). In addition, each façade orientation is subjected to different WDR loads depending on the wind direction co-occurring with rainfall events, which implies that different amounts of water get evaporated (Pérez et al., 2018, 2020b).

As a result, 96 h is arguably an arbitrary interval between WDR spells, thus resulting in spell indices that do not reliably characterise WDR exposure events reachable on building façades. Conversely, this 96-h model can be considered a simplistic climate-based index (Kubilay et al., 2021), which prioritises both a rapid and generic characterisation over accuracy.

This study aims to enhance the generic characterisation of WDR spells by effectively considering the influence of façade orientation and local climatic factors on their duration. To this end, an estimate of potential evaporation losses in façades has been proposed, combining commonly accepted formulae used in evapotranspiration studies and specific adaptations. To enhance the general applicability of the ISO standard, this approach also omits the properties of façade materials and simply considers weather records usually available together with those used in the 96-h ISO model.

Combining WDR exposure with potential evaporation losses, the transient wetting conditions at each façade can be generically assessed to permit: *(i)* characterising representative time intervals required for prior WDR loads to evaporate, *(ii)* determining façade-specific WDR spells linked to these intervals, and *(iii)* calculating spell indices that include the effect of orientation and local climatic factors on the characterisation of WDR exposure events.

In Section 2, the semi-empirical calculation established by the ISO standard is summarised, as is a specific combination of formulae used to estimate potential evaporation in evapotranspiration studies, endorsed by the Food and Agriculture Organization of the United Nations (FAO) and the American Society of Civil Engineers (ASCE) (EN ISO 15927-3, 2009; Allen et al., 1998; Walter et al., 2005). In Section 3, the specific adjustments and simplifications considered to functionally estimate potential evaporation on building façades are described. This study concludes by identifying and comparing façade-specific WDR spells on façades with varied orientations and climates, located at six sites in The

Netherlands and Southeast of Spain (Region of Murcia) (Peel et al., 2007). For this purpose, hourly WDR loads impinging on each façade orientation over a 10-year period (2010–2020) were quantified using the semi-empirical relationship established by ISO standard 15927-3. Throughout these years, the simultaneous potential evaporation losses of façades have also been characterised by means of the proposed method of estimation. In Section 4, these results are discussed and compared to those obtained by using the current 96-h ISO model.

2. Background

The semi-empirical relationship established in ISO standard 15927-3 determines the amount of WDR passing through a vertical surface in an undisturbed airstream, based on simultaneous climatic records collected every hour in airfield conditions (open field and 10 m above ground level). This relationship is used to inform indices that are determined from at least 10 years of measurements (EN ISO 15927-3, 2009; Blocken and Carmeliet, 2004; WMO, 2008). To quantify the WDR that reaches the façade orientation θ (°) during each spell $I'_{S\theta}$ (mm/spell) (Eq. (1)), only m hourly records of the following variables must be considered: wind speed U_{10} (m/s), wind direction D (°), and rainfall R_h (mm) related to the spell, and in which the wind direction affects the façade orientation being analysed (EN ISO 15927-3, 2009). This implies an identifiable calculation for each possible façade orientation, dismissing those results without a positive value in the summation (i.e. WDR not impinging on the façade orientation).

$$I'_{S\theta} = \frac{2}{9} \cdot \sum_{i=1}^{m} U_{10\,i} \cdot (R_{h\,i})^{8/9} \cdot \cos(D_i - \theta) \tag{1}$$

To obtain the characteristic spell index $I_{S\theta}$ (mm/spell), the most unfavourable $I'_{S\theta}$ value that can occur every three years is determined. For this calculation, the ISO standard proposes the 67th percentile of the $I'_{S\theta}$ values, although these traditional percentiles result in considerably underestimated exposure values as compared to those obtained by extreme value analyses (e.g. the Gumbel distribution) (Gumbel, 1958; Smith and Ledermann, 1990). Hence, the Gumbel distribution was used in this study to determine more realistic $I_{S\theta}$ values associated with a three-year occurrence (Eq. (2)).

$$\text{Probability}(x \geq \gamma) = 1 - \exp^{-\exp^{-(x-u_x)/\beta_x}} = \frac{1}{\text{return period (years)}} \tag{2}$$

The *Probability* ($x \geq \gamma$) that a given value γ of the variable x ($I'_{S\theta}$ values) is exceeded during a particular year depends only on the maximum annual $I'_{S\theta}$ values and the number of analysed years, where u_x and β_x are the mode and dispersion parameters of these series of maxima, respectively. This probability is inversely proportional to the return period associated with that value γ (i.e. 0.33 or 33% for a three-year period).

Given that each ISO spell ends invariably with an episode of 96 consecutive hours without WDR over the façade orientation, this constant interval determines the spell durations, maximum annual $I'_{S\theta}$ values, and resultant spell index $I_{S\theta}$. If the drying interval were actually longer, it would be more challenging for the conditions that lead to spell interruption to occur. Consequently, these spells would have a longer duration, resulting in a higher amount of accumulated WDR (i.e. greater $I'_{S\theta}$ values). On the contrary, a greater number of spells would be identified each year if the drying interval were shorter, with shorter durations and a lower amount of maximum accumulated WDR. It is therefore advisable to reliably identify the intervals required for the loss of moisture by evaporation to exceed the gain from prior WDR to establish spell durations, $I'_{S\theta}$ values, and spell indices suited to the actual façade conditions.

For this purpose, formulae commonly accepted in the field of evapotranspiration can be used as the starting point, which allows quantification of the potential evaporation losses associated with environmental conditions. Instead of a yearly based estimate of potential evaporation (as for climate-based indices and moisture reference years) (Zhou et al., 2016; Kubilay et al., 2021), this study utilises it to identify representative drying intervals (hours) required by building façades after each WDR exposure event.

2.1. Brief overview of the basic formulation to calculate potential evaporation loss

Evaporation occurs when liquid water turns into a vapour at a material surface. A continuous exchange of water molecules with vapour occurs at this evaporative surface. This exchange depends on the energy supply that provides the latent heat of vaporisation and the ease with which vapour can diffuse away from the evaporative surface (Penman, 1948). To represent both factors, the most widespread model (Penman Model) uses a combination of an energy balance term based on the principles of the energy budget and an aerodynamic term based on the vapour pressure deficit and wind speed near the surface (Eq. (3)). The influence of both evaporation components ($E_{radiative}$ and $E_{aerodynamic}$) on the potential evaporation E (mm/time) is determined by the slope of the saturation vapour pressure-temperature relationship Δ (kPa/°C) and the psychrometric constant γ (kPa/°C) (Penman, 1948; Shirsath and Singh, 2010).

$$E = \frac{\Delta}{\Delta + \gamma} \cdot E_{radiative} + \frac{\gamma}{\Delta + \gamma} \cdot E_{aerodynamic} \tag{3}$$

A more detailed insight into the climatic factors involved in both components can be inferred from the Penman–Monteith form of this model (Eq. (4)), which is commonly used to characterise crop evapotranspiration by specifically adjusting its variables (Allen et al., 1998). In Eq. (4), R_n represents the net radiation, G is the soil heat flux, λ is the latent heat of vaporisation, ρ_a represents the mean air density at constant pressure, 0.622 denotes the ratio of molecular weight of water vapour to dry air, (P_{sat} - P_v) represents the vapour pressure deficit of the air, P is the atmospheric pressure, and r_a is the aerodynamic resistance.

$$E = \frac{\Delta}{\Delta + \gamma} \cdot \left(\frac{R_n - G}{\lambda} \right) + \frac{\gamma}{\Delta + \gamma} \cdot \left(\frac{\rho_a \cdot 0.622}{P} \cdot \frac{P_{sat} - P_v}{r_a} \right) \tag{4}$$

This potential evaporation loss can be adjusted by adopting suitable variables such as albedo, crop height, roughness length governing transfer of heat and vapour, and active (sunlit) leaf area (Shuttleworth and Maidment, 1993; Allen et al., 1998). However, a neutral characterisation of potential evaporation is required for this study, free from biases related to the study of crops. Suttleworth (Shuttleworth and Maidment, 1993) re-wrote this equation in metric units by adopting an appropriate form of r_a for open water evaporation, standardised weather measurements collected at a height of 2 m, and a roughness length equal to 0.00137 m (the same value implicitly assumed by Penman). For hourly calculations, the potential evaporation loss E (mm/h) can be determined using Eq. (5) as a function of the net radiation exchange at the free water surface R_n (expressed in equivalent mm/h), the energy advected to the evaporative surface G (also expressed in mm/h), the wind speed U_2 (m/s) recorded at a height of 2 m, the vapour pressure deficit P_{sat} - P_v (kPa), and the air temperature T (°C). The latent heat of vaporisation λ can be estimated from the air temperature as *2.501-0.002361 T* or, otherwise, be adopted a constant value equal to 2.45 MJ/kg (Shuttleworth and Maidment, 1993; Allen et al., 1998). The conversion of energy values (e.g. R_n and G) into depths of water is given by the division of the energy term (MJ/m^2) by the latent heat of vaporisation and water density (1000 kg/m^3). Thus, considering a constant λ value of 2.45 MJ/kg, 1 MJ/m^2·h would be equivalent to 0.408 mm/h. The resulting potential evaporation represents an ideal situation, in which the inner nature of the evaporative surface is ignored.

$$E = \frac{\Delta}{\Delta + \gamma} \cdot (R_n - G) + \frac{\gamma}{\Delta + \gamma} \cdot \left(\frac{6.43 \cdot (1 + 0.536 \cdot U_2) \cdot (P_{sat} - P_v)}{24 \cdot (2.501 - 0.002361 \cdot T)} \right) \tag{5}$$

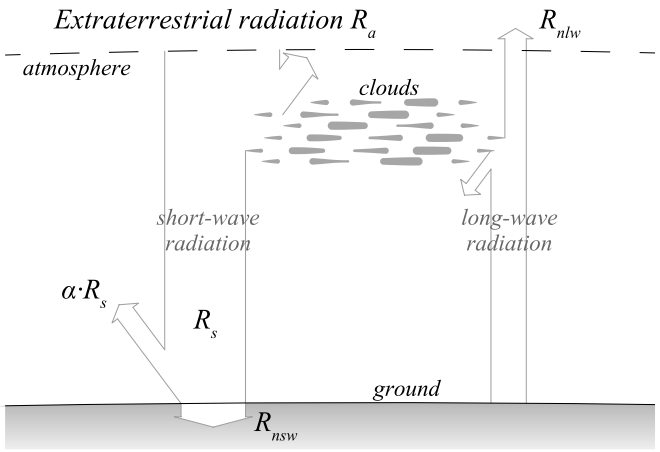

Fig. 2. Summary of radiation components usually considered during evapotranspiration.

The slope of the saturation vapour pressure-temperature relationship Δ (kPa/°C) can be obtained from the air temperature T (°C) and the saturation vapour pressure P_{sat} (kPa) using Eq. (6). In turn, the psychrometric constant γ (kPa/°C) adopts a value based on the atmospheric pressure P (kPa) when λ equals 2.45 MJ/kg: $\gamma = 0.000665\ P$ kPa/°C (Allen et al., 1998; Walter et al., 2005).

$$\Delta = \frac{4098[P_{sat}]}{(T+237.3)^2} \approx \frac{4098\left[0.6108 \cdot \exp\left(\frac{17.27 \cdot T}{T+237.3}\right)\right]}{(T+237.3)^2} \tag{6}$$

To convert conventional wind speed records gathered at weather stations (commonly at a height of 10 m above ground level) into agro-meteorological records collected at a height of 2 m, a logarithmic wind speed profile is often used (Eq. (7)), where U_2 (m/s) is the agro-meteorological wind speed and U_z (m/s) represents the weather record at height z (m) (Allen et al., 1998; Walter et al., 2005).

$$U_2 = U_Z \frac{4.87}{\ln(67.8 \cdot z - 5.42)} \tag{7}$$

If the energy term of the general equation is addressed (Eq. (5)), the net radiation R_n (MJ/kg·h) absorbed by the surface can be defined as the difference between the net incoming shortwave radiation R_{nsw} and net outgoing longwave radiation R_{nlw} (Eq. (8)) (Allen et al., 1998; Walter et al., 2005; An et al., 2017; Evett et al., 2011). The shortwave radiation that is not scattered, reflected, or absorbed by the atmosphere constitutes the solar radiation on a horizontal plane R_s (MJ/m^2·h), which is usually available as part of the weather records. In turn, a fraction of this solar radiation is reflected by the evaporative surface, depending on its characteristics and the angle of incidence of the solar beams (Oke, 1987; Krayenhoff and Voogt, 2010). This fraction is commonly assessed as a constant value, known as albedo ρ. Therefore, the net incoming shortwave radiation R_{nsw} represents the fraction of R_s not reflected by the evaporative surface.

$$R_n = R_{nsw} - R_{nlw} = R_s - \rho \cdot R_s - R_{nlw} \tag{8}$$

For its part, the Earth's surface emits longwave radiation that warms the atmosphere, causing the atmosphere to also emit longwave radiation. Thus, each evaporative surface emits and receives longwave radiation, resulting in a net longwave radiation R_{nlw} (MJ/m^2·h) that normally causes energy loss (Fig. 2). The R_{nlw} value can be estimated from the Stefan–Boltzmann law by applying corrections to consider the influence of humidity and cloudiness as atmospheric absorbers (Eq. (9)) (Allen et al., 1998; Walter et al., 2005; An et al., 2017; Evett et al., 2011). In this equation, σ expresses the Stefan–Boltzmann constant ($2.042 \cdot 10^{-10}$ kJ/K^4·m^2·h), T (K) is the mean air temperature during the considered interval (1-h intervals in this study), the term in parentheses represents the surface net emittance by considering the actual vapour pressure P_v (kPa), and f_{cloud} indicates the effect of cloudiness. Vapour pressure P_v can be obtained from weather records of relative humidity and P_{sat} values (see Eq. (6)).

$$R_{nlw} = \sigma \cdot T^4 \cdot \left(0.34 - 0.14 \cdot \sqrt{P_v}\right) \cdot f_{cloud} \tag{9}$$

The ratio R_s/R_{so} included in the f_{cloud} term is the fraction of radiation under clear-sky conditions R_{so} that reaches the Earth's surface (Eq. (10)). This ratio is limited between 0.3 (dense cloud) and 1 (cloudless conditions), so any lower and higher values should be truncated. Therefore, the f_{cloud} value ranges from 0.055 to 1.0 (Walter et al., 2005; Jensen et al., 1990).

$$f_{cloud} = 1.35 \cdot \frac{R_s}{R_{so}} - 0.35 \tag{10}$$

The solar radiation in the case of clear-sky R_{so} (MJ/m^2·h) can be estimated using Eq. (11), where z (m) represents the altitude of the analysed location and R_a (MJ/m^2·h) is the amount of extraterrestrial radiation (Allen et al., 1998; Walter et al., 2005; An et al., 2017). By definition, both R_{so} and R_a values are equal 0 during the night, and f_{cloud} value remains undefined.

$$R_{so} = (0.75 + 0.00002 \cdot z) \cdot R_a \tag{11}$$

As presented in Eq. (12), the amount of extraterrestrial radiation for hourly intervals R_a (MJ/m^2·h) can be calculated from the solar constant G_{SC} (4.92 MJ/m^2·h), the inverse relative distance Earth-Sun d_r, the location latitude ρ (rad) -positive values for the Northern Hemisphere-, the solar declination δ (rad), and the solar time angle at the beginning and the end of the considered hourly interval w_1 (rad) and w_2 (rad), respectively (Duffie and Beckman, 2013; Allen et al., 1998; Walter et al., 2005; An et al., 2017; Evett et al., 2011; Jensen et al., 1990).

$$R_a = \frac{12}{\pi} \cdot G_{SC} \cdot d_r \cdot [(w_2 - w_1) \cdot \sin\rho \cdot \sin\delta + \cos\rho \cdot \cos\delta \cdot (\sin w_2 - \sin w_1)] \tag{12}$$

Both solar declination and inverse relative distance Earth-Sun can be obtained from the ordered number J of the day in year using Eq. (13) (J = 1 for 1 January and J = 365 or 366 for 31 December). Subsequently, the constant d_r and δ values can be used for all hours on the same day (Allen et al., 1998; Walter et al., 2005).

$$\begin{aligned} d_r &= 1 + 0.033 \cdot \cos\left(\frac{2 \cdot \pi \cdot J}{365}\right) \\ \delta &= 0.409 \cdot \sin\left(\frac{2 \cdot \pi \cdot J}{365} - 1.39\right) \end{aligned} \tag{13}$$

w_1 and w_2 values were defined around the solar time angle at the midpoint of the interval w (rad), where t_h (h) is the length of the considered interval (Eq. (14)) (An et al., 2017; Evett et al., 2011). According to the standards established by FAO and ASCE (Allen et al., 1998; Walter et al., 2005), this solar time angle w is determined by the standard hour of the day (clock time) at the interval midpoint t (h), the longitude of the centre of the local time zone L_z (rad), and the longitude of the location L_m (rad), both longitudes considering positive values west of Greenwich, and the seasonal correction of solar time S_c (h). It should be noted that the values of w (rad) have negative values during the first part of the day and positive values after noon.

$$\begin{aligned} w_1 &= w - \frac{\pi \cdot t_h}{24} \\ w_2 &= w + \frac{\pi \cdot t_h}{24} \\ w &= \frac{\pi}{12}\left[\left(t + \frac{4}{60} \cdot (L_z - L_m) + S_c\right) - 12\right] \end{aligned} \tag{14}$$

The seasonal correction of solar time S_c shown in Eq. (15) represents a simplified form of the equation of time and can be used with reduced effort and considerable accuracy (the error does not exceed 88 s regarding the extended equation of time) (Evett et al., 2011; Jensen et al., 1990).

$$S_c = 0.1645 \cdot \sin(2 \cdot b) - 0.1255 \cdot \cos b - 0.025 \cdot \sin b$$
$$b = \frac{2 \cdot \pi \cdot (J - 81)}{364} \quad (15)$$

The formula that determines the extraterrestrial radiation at hourly intervals (Eq. (12)) lacks physical sense during hours in which the sun is below the horizon. The solar time angle linked to sunrise and sunset $w_{sunrise/sunset}$ (rad) can be determined for each location and solar declination during the year from Eq. (16) (Duffie and Beckman, 2013; An et al., 2017; Evett et al., 2011). Accordingly, hourly intervals with w_2 values less than -$w_{sunrise/sunset}$ must be discarded (i.e. before sunrise) as well as those intervals with w_1 values greater than $w_{sunrise/sunset}$ (at night). An R_a value equal to 0 should be considered for all these hours. During the hour of sunrise, the w_1 value resulting from Eq. (14) must be replaced with -$w_{sunrise/sunset}$. Similarly, in the interval w_1-w_2 in which sunset occurs, the w_2 value should be replaced with $w_{sunrise/sunset}$ (Walter et al., 2005).

$$w_{sunrise/sunset} = \text{acos}(\tan \rho \cdot \tan \delta) \quad (16)$$

Furthermore, R_s values in the weather records usually contain small errors associated with the out-of-level of the pyranometer and imperfect corrections of the instrument cosine error. These errors are irrelevant throughout most of the day when the solar radiation is large. However, these imperfections cause significant percentage variations when the sun angle above horizon β (rad) is small (see Eq. (17)), that is, near dawn and in the evening, given the low R_s values associated with both moments (Duffie and Beckman, 2013; Walter et al., 2005). Because the R_a value expresses a theoretical estimation that is not disrupted by instrumental defects, Eq. (10) may yield unreliable values despite the limitation imposed on the R_s/R_{so} ratio (between 0.3 and 1.0).

$$\beta = \text{asin}(\sin \rho \cdot \sin \delta + \cos \rho \cdot \cos \delta \cdot \cos w) \quad (17)$$

For this reason, the f_{cloud} values during hourly intervals with $\beta < 0.3$ rad (after sunrise and in the evening) should be replaced with the immediately prior f_{cloud} value associated with a β value higher or equal to 0.3 rad (Walter et al., 2005). In locations with high latitudes and in certain months of the year, the sun may not reach an angle above the horizon higher than 0.3 rad throughout the entire day. For these days (from sunrise to the next sunrise), a representative average of all the R_s/R_{so} values identified during the day has been adopted, although none of them met the $\beta > 0.3$ requirement.

Finally, the energy advected to the evaporative surface G (e.g. the soil heat flux if evapotranspiration is considered) expresses the part of the energy used to heat the material. The energy gained or lost by the evaporative surface should be subtracted or added, respectively, to R_n when estimating potential evaporation loss (G with positive value when the surface is warming and negative value when it is cooling). For hourly intervals and evapotranspiration applications, G is commonly estimated as a percentage value of R_n ranging from 0.1 to 0.5 (Allen et al., 1998; Walter et al., 2005).

3. Methods

The previous base formulation has been adjusted to calculate evapotranspiration rate for a grass reference crop, as well as any other particular crop (Shuttleworth and Maidment, 1993; Allen et al., 1998; Walter et al., 2005). However, assessing the potential evaporation on tilted surfaces (90° in the most common case of building façades) and with varied orientations requires specific adaptations, in addition to assuming some hypotheses that allow the functional estimation of the net longwave radiation and heat flux of the façade. The proposed adaptations and assumptions are as follows:

3.1. Characterisation of potential evaporation on vertical façades with varied orientations

The first task was in estimating the shortwave radiation that the façade receives based on the available R_s measured on a horizontal plane. Unlike a horizontal surface, part of the overall radiation incident on the façade comes from the shortwave radiation reflected from nearby surfaces (i.e. $\alpha \cdot R_s$). In addition, the vertical surface receives direct (beam) radiation and diffuse radiation scattered or reflected by water vapour, dust, and pollution present in the atmosphere (which cannot be focused). In this regard, it should be clarified that the R_s radiation measured at many weather stations is the sum of both direct and diffuse radiation on a horizontal surface ($R_s = R_{s\ direct} + R_{s\ diffuse}$) (Maleki et al., 2017).

In instances for which the available weather records do not comprise this differentiate between hourly diffuse and direct solar radiation on horizontal surfaces, various mathematical models have been proposed to distinguish between these two radiation components. One of the most used functional approach establishes a proportional relationship (K_D factor) between diffuse and measured radiation (Maleki et al., 2017). K_D varies depending on the time of the year, atmospheric absorbers, climatic conditions, location, etc. All of these parameters can be jointly expressed as a generic clearness index K_T, defined as the ratio between the solar radiation measured by the pyranometer and the amount of extraterrestrial radiation R_a calculated in the same interval. Thus, every hour, it is possible to identify the K_T value and, consequently, the diffuse radiation $R_{s\ diffuse}$ that is present in the measured radiation R_s. Owing to its simplicity, the decomposition model proposed by Erbs et al. (1982) was used in this study, which was validated from hourly experimental records collected in the USA at latitudes between 31° and 42° (Eq. (18)). In any case, other models can also be proposed, provided that they have been validated under climatic conditions similar to those of the locations to be analysed.

$$R_{s\ diffuse} = K_D \cdot R_s$$
$$K_{D\ (K_T \le 0.22)} = 1 - 0.09 \cdot K_T$$
$$K_{D\ (0.22 < K_T \le 0.80)} = 0.9511 - 0.1604 \cdot K_T + 4.388 \cdot K_T^2 - 16.638 \cdot K_T^3 + 12.336 \cdot K_T^4$$
$$K_{D\ (K_T > 0.80)} = 0.165$$
$$K_T = \frac{R_s}{R_a} \quad (18)$$

Once the diffuse component of R_s has been obtained, the influence of each radiative component (direct, diffuse, and reflected) over the vertical façade can be quantified. Eq. (19) presents a quantification of these three radiative components on tilted surfaces based on the anisotropic model proposed by Hay, which differentiates between circumsolar and uniform diffuse radiation throughout the celestial dome (Hay, 1979). The conversion factors C_{dir}, C_{dif}, and C_{ref} are related to the contribution of direct radiation $R_{s\ direct}$ (MJ/m^2·h), diffuse radiation $R_{s\ diffuse}$ (MJ/m^2·h), and reflected radiation from the ground $\alpha \cdot R_s$ (MJ/m^2·h), respectively (Duffie and Beckman, 2013; Ronoh and Shamshiri, 2021). C_{dif}, and C_{ref} depend on the surface inclination (adopted here as 90° or equivalently $\pi/2$ rad) and are equal to $0.5 \cdot (1 + \cos(\pi/2))$ and $0.5 \cdot (1 - \cos(\pi/2))$, respectively.

$$R_{s\ 90^\circ} = C_{dir} \cdot R_{s\ direct} + C_{dir} \cdot \frac{R_{s\ direct}}{R_a} \cdot R_{s\ diffuse} + C_{dif} \cdot \left(1 - \frac{R_{s\ direct}}{R_a}\right) \cdot R_{s\ diffuse} + C_{ref} \cdot \alpha \cdot R_s \quad (19)$$

In turn, C_{dir} is a geometrical factor that varies throughout the day (Eq.

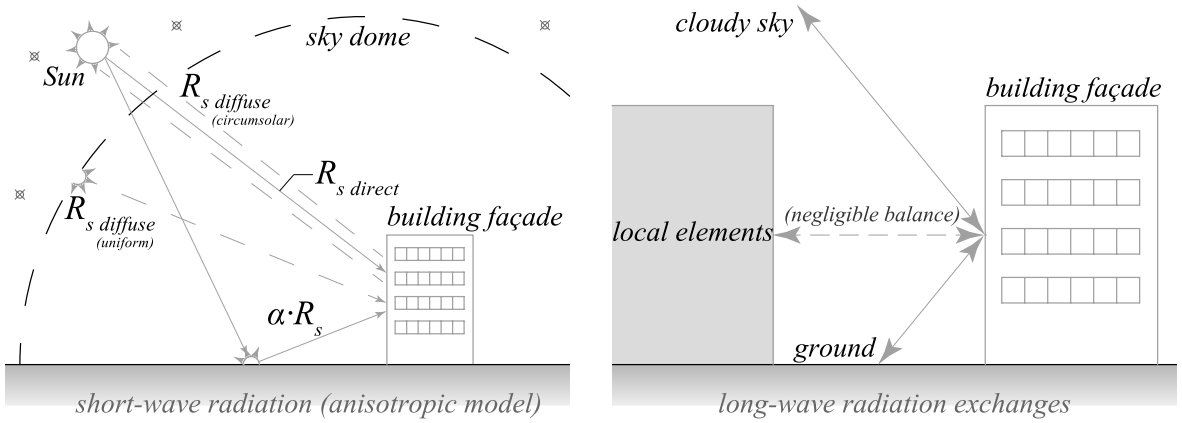

Fig. 3. Schemes of shortwave radiation sources (direct, diffuse, and reflected) and longwave radiation exchanges considered for the tilted surface.

(20)) and refers to the ratio between the cosine of the incident angle of the solar beams on the vertical surface φ_{90° (rad) and the cosine of the incident angle on the horizontal surface -solar zenith angle- φ_{0° (rad). In this equation, the façade tilt was also directly replaced with its conventional value (π/2 rad). In turn, ψ (rad) represents the solar azimuth angle of the façade with respect to the Sun, with positive values west of south and negative values east of south (south equals to 0 and north to π rad) (Klein and Theilacker, 1981). As can be deduced, negative incidence angles and greater than π/2 rad indicate that there is no direct solar radiation on the façade during these hourly intervals. Eq. (20) can be simplified by replacing the terms cos(π/2) and sin(π/2) by 0 and 1, respectively.

$$
\begin{aligned}
C_{dir} &= \frac{\cos\varphi_{90^\circ}}{\cos\varphi_{0^\circ}} = \frac{A\cdot\cos w - B + C\cdot\sin w}{\cos w - \cos w_{sunrise/sunset}} \\
A &= \cos\frac{\pi}{2} + \tan\rho\cdot\cos\psi\cdot\sin\frac{\pi}{2} \\
B &= \cos w_{sunrise/sunset}\cdot\cos\frac{\pi}{2} + \tan\delta\cdot\sin\frac{\pi}{2}\cdot\cos\psi \\
C &= \frac{\sin\frac{\pi}{2}\cdot\sin\psi}{\cos\rho}
\end{aligned}
\tag{20}
$$

Depending on the façade orientation, the moments at which direct radiation begin and end need not be symmetrical about solar noon, nor does it correspond to the solar time angle associated with sunrise/sunset on horizontal surfaces (see Eq. (16)). Therefore, Eq. (21) was required to calculate the solar time angles $w_{sunrise\ 90^\circ}$ and $w_{sunset\ 90^\circ}$ (rad) linked to the effective sunrise and sunset moments on the façade orientation (Klein and Theilacker, 1981). As detailed, the signs of Eq. (21) are affected by the façade orientation. Those hourly intervals with w_2 values less than $w_{sunrise\ 90^\circ}$ must be discarded as along with those with w_1 values greater than $w_{sunset\ 90^\circ}$.

$$
\begin{aligned}
|w_{sunrise\ 90^\circ}| &= \min\left\{ w_{sunrise/sunset}; \operatorname{acos}\left[\frac{A\cdot B + C\cdot\sqrt{A^2 - B^2 + C^2}}{A^2 + C^2}\right]\right\} \\
w_{sunrise\ 90^\circ} &= \begin{matrix} -|w_{sunrise\ 90^\circ}| \text{ if } (A>0 \text{ and } B>0) \text{ or } (A\geq B) \\ +|w_{sunrise\ 90^\circ}| \text{ otherwise} \end{matrix} \\
|w_{sunset\ 90^\circ}| &= \min\left\{ w_{sunrise/sunset}; \operatorname{acos}\left[\frac{A\cdot B - C\cdot\sqrt{A^2 - B^2 + C^2}}{A^2 + C^2}\right]\right\} \\
w_{sunset\ 90^\circ} &= \begin{matrix} +|w_{sunset\ 90^\circ}| \text{ if } (A>0 \text{ and } B>0) \text{ or } (A\geq B) \\ -|w_{sunset\ 90^\circ}| \text{ otherwise} \end{matrix}
\end{aligned}
\tag{21}
$$

Furthermore, unrepresentative values of C_{dir} may be obtained in hours that include sunrise and sunset owing to the negligible cos φ_{0° values associated with these hours (Eq. (20)). These negligible values can cause extremely high C_{dir} values, resulting in direct radiation estimates that do not correspond to the reality of these hourly intervals (Duffie and Beckman, 2013). To prevent unreliable values for direct radiation in those hours, a limit of the values of $C_{dir} \leq 10$ was adopted.

Once the radiation on the façade orientation $R_{s\ 90^\circ}$ (MJ/m^2·h) was identified, the net radiation $R_{n\ 90^\circ}$ (MJ/m^2·h) was obtained using Eq. (22), by quantifying the reflected radiation and its longwave radiation exchange $R_{nlw\ 90^\circ}$ (MJ/m^2·h). To determine the reflected radiation, a constant albedo ρ equal to 0.2 was suggested as a representative value of different albedos already identified in urbanised surroundings (Oke, 1987; Krayenhoff and Voogt, 2010; Trlica et al., 2017).

$$
R_{n\ 90^\circ} = R_{s\ 90^\circ} - \rho\cdot R_{s\ 90^\circ} - R_{nlw\ 90^\circ} \tag{22}
$$

The second task was estimating the longwave radiation exchange $R_{nlw\ 90^\circ}$ of the building façade. For this, the Stefan–Boltzman law was used, which determines the radiant emittance as the product of the effective emissivity ε, the constant of proportionality σ ($2.042\cdot10^{-10}$ MJ/K^4·m^2·h), and the surface temperature T (K) to the fourth power (for example, refer to Eq. (9)) (An et al., 2017; Delgado et al., 2010; Künzel et al., 2002). As presented in Fig. 3, the longwave radiation exchange at a vertical surface can be described as the sum of the exchange with the surrounding ground, sky, and other local elements (e.g. buildings and trees) (Ronoh and Shamshiri, 2021).

To assess this radiation exchange, the usual assumption that the sky behaves as a grey body was maintained, considering an effective sky emissivity value that permits the use of air temperature records near the ground (Convertino et al., 2020). Similarly, it was assumed that the ground temperature was equal to the external air temperature (Delgado et al., 2010; EN ISO 52016-1, 2017). For practicality, it was also considered that the surrounding surfaces (mostly other façades in an urban context) have a temperature similar to that of the façade being analysed, and therefore, the net exchange of energy between them is negligible. Each energy exchange is weighted by a view factor that represents the field-of-view from a base surface obstructed by a given surface (Duffie and Beckman, 2013; Delgado et al., 2010; EN ISO 52016-1, 2017).

Based on these hypotheses, the net exchange of longwave radiation on the building façade $R_{nlw\ 90^\circ}$ (MJ/m^2·h) was estimated by means of Eq. (23), where $\varepsilon_{façade}$ is the façade emissivity, $T_{façade}$ (K) is the temperature of the façade surface, $\varepsilon_{cloudy\text{-}sky}$ is the effective atmospheric emissivity, adding the impact of cloudiness, T (K) is the external air temperature, and ε_{ground} is the ground emissivity. For consistency, the conversion factors previously considered in Eq. (19) were adopted as view factors: 0.5·(1 + cos(π/2)) for the view factor to the sky and 0.5·(1-cos(π/2)) for the view factor to the ground. Therefore, both terms may be replaced by 0.5 to simplify Eq. (23).

$$
\begin{aligned}
R_{nlw\ 90^\circ} = &\frac{1+\cos\frac{\pi}{2}}{2}\cdot\left(\sigma\cdot\varepsilon_{façade}\cdot T_{façade}{}^4\right. \\
&\left. - \sigma\cdot\varepsilon_{cloudy\ sky}\cdot T^4\right) + \frac{1-\cos\frac{\pi}{2}}{2}\cdot\left(\sigma\cdot\varepsilon_{façade}\cdot T_{façade}{}^4 - \sigma\cdot\varepsilon_{ground}\cdot T^4\right)
\end{aligned}
\tag{23}
$$

With regard to emissivity values, two constant values were generically adopted for both the ground and façades, which allows the results obtained at different locations to be compared. Nevertheless, both emissivity values could be adjusted to better represent particular case studies. Thus, an $\varepsilon_{façade}$ value of 0.910 was suggested as a representative value of those multiple façade materials already identified (Oke, 1987; Künzel et al., 2002; J.H. Liendhard IV and J.H. Liendard V, 2020). In turn, $\varepsilon_{ground} = 0.974$ was used as a common value for urban areas (Mira et al., 2017; Wittich, 1997).

To determine $\varepsilon_{cloudy\text{-}sky}$, an empirical model based on the sky emissivity correlations proposed by Berdahl and Martin was chosen (Eq. (24)) (Berdahl and Martin, 1984; Algarni and Nutter, 2015). In this model, the emissivity of the cloudy-sky $\varepsilon_{cloudy\ sky}$ was calculated from the clear-sky emissivity value $\varepsilon_{clear\text{-}sky}$ and from the f_{cloud} factor presented in Eq. (10). In turn, the $\varepsilon_{clear\text{-}sky}$ value was estimated using a quadratic function, empirically obtained from 57 months of records gathered in the USA (Convertino et al., 2020; Berdahl and Martin, 1984). This quadratic function depends on the dew point temperature of the air T_{dp} (K), which is determined from its vapour pressure P_v (kPa) (Convertino et al., 2020; Karn et al., 2019). In Eq. (24), the original quadratic function used for the monthly data was adjusted to consider the impact of the time of day t (h) and the effect of atmospheric pressure P (kPa) on sky emissivity, thus allowing an hourly calculation (Zhang et al., 2017). Alternatively, other models for cloudy-sky emissivity can be proposed if they are deemed to be more representative of the location being analysed.

For this study, a R_{se} value equal to 0.04 m^2 K/W was used as well as an indoor comfort temperature of 20 °C (i.e. 293.15 K) throughout the year, following the guidelines established by the Spanish Technical Building Code and the ISO standard 6946 (EN ISO 6946, 2021; Spanish Ministry of Development, 2022). The minimum R-value required for façades by each national or regional building regulation is suggested as the R_{total} value, thus achieving conservative results. The external air temperature was available as hourly weather records.

The last task to be addressed was quantifying the heat flux G associated with the building façades. For evapotranspiration applications, this heat flux can be empirically parameterised by means of soil thermal conductivity and temperatures at two known depths (Cammalleri et al., 2009). An analogous approach was proposed to approximate the $G_{façade}$ value (MJ/m^2·h) based on the façade R_{total} value (m^2·K/W) and the difference between the indoor temperature T_{int} (K) and façade temperature $T_{façade}$ (K) (Eq. (26)). The constant of 0.0036 in Eq. (26) allowed the conversion of W/m^2 to MJ/m^2·h. Again, the minimum R-value required for façades at each location is employed as the R_{total} value. When using this approach, both the soil and façades are acknowledged to receive continuous energy inputs that were ignored in the energy budget (geothermal energy for evapotranspiration and air conditioning for buildings), which allows maintaining an unlimited heat flux.

$$G_{façade} = \frac{T_{façade} - T_{\text{int}}}{R_{total}} \cdot 0.0036 \tag{26}$$

Finally, it should be noted that the wind speed varies according to the height of the façade, which made it convenient to convert wind speeds to the height of each façade (Eq. (7)). In this regard, wind speed values at a height of 10 m were used in Eq. (5), thus homogenising the aerodynamic term used for horizontal surfaces to the reference height also considered for the WDR calculation.

$$\begin{aligned}
&\varepsilon_{cloudy\ sky} = \varepsilon_{clear\ sky} + 0.9 \cdot \left(1 - \varepsilon_{clear\ sky}\right) \cdot f_{cloud} \\
&\varepsilon_{clear\ sky} = 0.711 + 0.56 \cdot \left(\frac{T_{dp} - 273.15}{100}\right) + 0.73 \cdot \left(\frac{T_{dp} - 273.15}{100}\right)^2 + 0.013 \cdot \cos\left(\frac{2 \cdot \pi \cdot t}{24}\right) + 0.00012 \cdot (10 \cdot P - 1000) \\
&T_{dp} = \frac{243.12 \cdot \ln\left(\frac{P_v}{0.6112}\right)}{17.62 - \ln\left(\frac{P_v}{0.6112}\right)} + 273.15
\end{aligned} \tag{24}$$

To determine the surface façade temperature $T_{façade}$ (K) related to each hourly interval, a simple analytical calculation was proposed (Eq. (25)), by combining the indoor temperature T_{int} (K), thermal resistance of the whole façade R_{total} (m^2·K/W), and external surface thermal resistance of the façade R_{se} (m^2·K/W). To account for the radiation effect on this surface temperature, the well-known concept of sol-air temperature $T_{sol\text{-}air}$ (K) is included. This temperature can be inferred based on the external air temperature T (K), façade absorptivity α (considered as the inverse value of the previously established albedo), external surface thermal resistance of the façade, and hourly shortwave radiation $R_{s\ 90^\circ}$ (W/m^2) on the façade (Marino et al., 2018). Alternative models can also be used to include this radiation effect (Charisi et al., 2018), as long as they do not require exhaustively characterising the properties of the façade materials. In this manner, the general applicability of the ISO standard and the general comparison of spell indices regardless of the façade configuration can be maintained. Since the temperature of the façade surface may exceed that of the external air, this façade temperature should also be used in Eqs. (5) and (6), thus considering the actual conditions of the boundary layer where the evaporation phenomenon occurs.

$$T_{façade} = T_{sol-air} + \frac{R_{se}}{R_{total}} \cdot \left(T_{\text{int}} - T_{sol-air}\right) = T + \alpha \cdot R_{s\ 90^\circ} \cdot R_{se} + \frac{R_{se}}{R_{total}} \cdot (T_{\text{int}} - T - \alpha \cdot R_{s\ 90^\circ} \cdot R_{se}) \tag{25}$$

By compiling the energy terms obtained from Eqs. (22) and (26) ($R_{n\ 90^\circ}$ and $G_{façade}$, respectively), the hourly potential evaporation E (mm/h) on building façades can be characterised by applying Eq. (5). For this, both energy values were converted into depths of water (1 MJ/m^2·h = 0.408 mm/h by assuming a constant latent heat of vaporisation of 2.45 MJ/kg). This hourly estimate of potential evaporation was thus compared with the hourly WDR loads that affect each façade to assess general wetting conditions over time. All the previous formulae were analytical in nature and could be easily implemented by means of typical spreadsheets, without requiring specialised modelling. It must also be remembered that the signs of the formulation must be adjusted accordingly for façade analyses performed in the Southern Hemisphere. Part of the formulation can also be simplified if exhaustive weather records are available (e.g. distinguishing between direct and diffuse radiation), using processed input data available from various sources (e.g. European Centre for Medium-Range Weather Forecasts), or resorting to specific software that can analyse the radiative components of specific façades in a complex urban environment (Hersbach et al., 2023; Blender Online Community, 2023).

Nevertheless, the use of Eq. (5) in façades does not remove all the

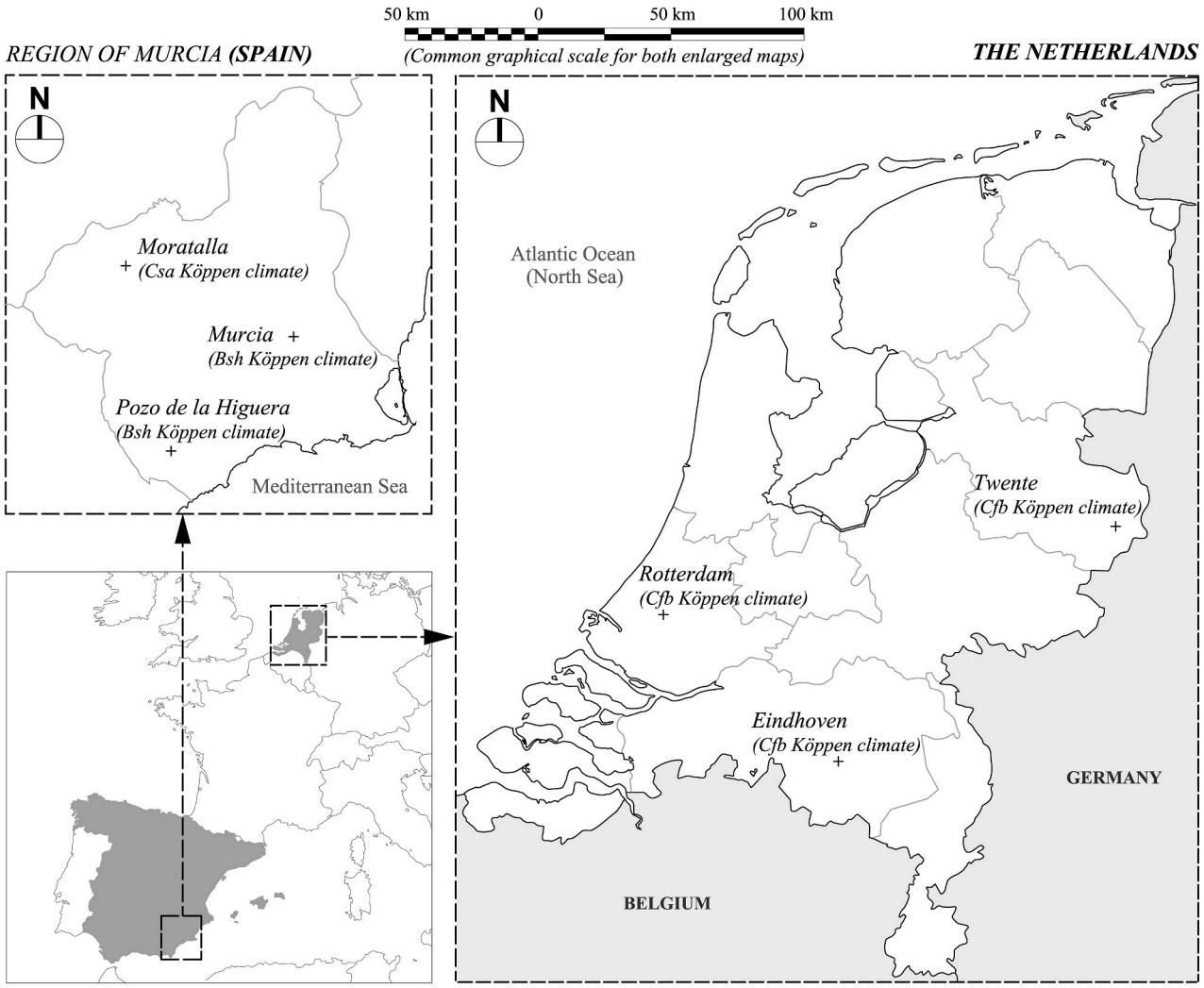

Average data **Stations**	**Latitude** *(DD)*	**Longitude** *(DD)*	**Altitude** *(m)*	**Missing data** *(%)*	R_h *(mm/yr)*	U_{10} *(m/s)*	**T** *(°C)*	**Relative humidity** *(%)*	R_s *(MJ/m²·yr)*
Einhoven **(NL)**	5.377	51.451	23	8.7	743.0	3.7	11.0	78.5	3,883.9
Twente **(NL)**	6.891	52.274	35	9.5	758.6	3.5	10.3	80.0	3,756.5
Rotterdam **(NL)**	4.447	51.962	-4	8.6	890.3	4.3	10.9	80.6	3,871.0
*Pozo de la Higuera***(ES)**	-1.699	37.671	337	0.4	198.1	2.3	16.9	64.8	18,447.6
Murcia **(ES)**	-1.133	37.933	60	0.0	287.4	0.9	18.9	55.9	18,203.5
Moratalla **(ES)**	-1.891	38.186	633	0.6	362.1	2.0	16.2	60.6	18,015.5

Fig. 4. Geographic distribution and main characteristics of the analysed weather stations.

uncertainties previously stated. On the one hand, the influence of the inner structure of the material on the water adsorption-desorption mechanisms that condition the evaporation phenomenon was not considered. On the other hand, apart from the significant simplifications introduced in the formulation, the roughness length implicitly considered by Suttleworth and Penman would not represent that which might exist on the façade surface and the existence of local shadows could also affect the energy balance. In this regard, the authors must emphasise that the objective of the proposed approach is not to perfectly quantify the evaporation balance for each type of façade. As was the case for evapotranspiration and the development of climate-based indices, the proposed approach is intended to provide a generic estimate of potential evaporation loss from façades thereby allowing more reliable generic spells to be identified, and thus permitting comparisons of values for evaporation loss.

3.2. Data analysis

Directional WDR exposure and proposed characterisation of potential evaporation at six weather stations located in The Netherlands and southwest of Spain (Region of Murcia) were analysed. The selected regions provide an evident contrast in climatic conditions. The Netherlands presents an oceanic climate dominated by Atlantic winds (Cfb according to the Köppen climate classification), whereas the Region of Murcia is characterised by climates ranging from the Mediterranean in the mountainous northwest of the region (Csa) to the Hot desert on the southwest coast (BWh), with a predominance of semi-arid climates (BsK and Bsh) (Peel et al., 2007; Chazarra et al., 2018).

Hourly records corresponding to rainfall intensity, wind velocity at a height of 10 m, air temperature, solar radiation, and relative humidity were used as input data for the proposed method. All these data were gathered by official institutions at these stations during 10 years (from

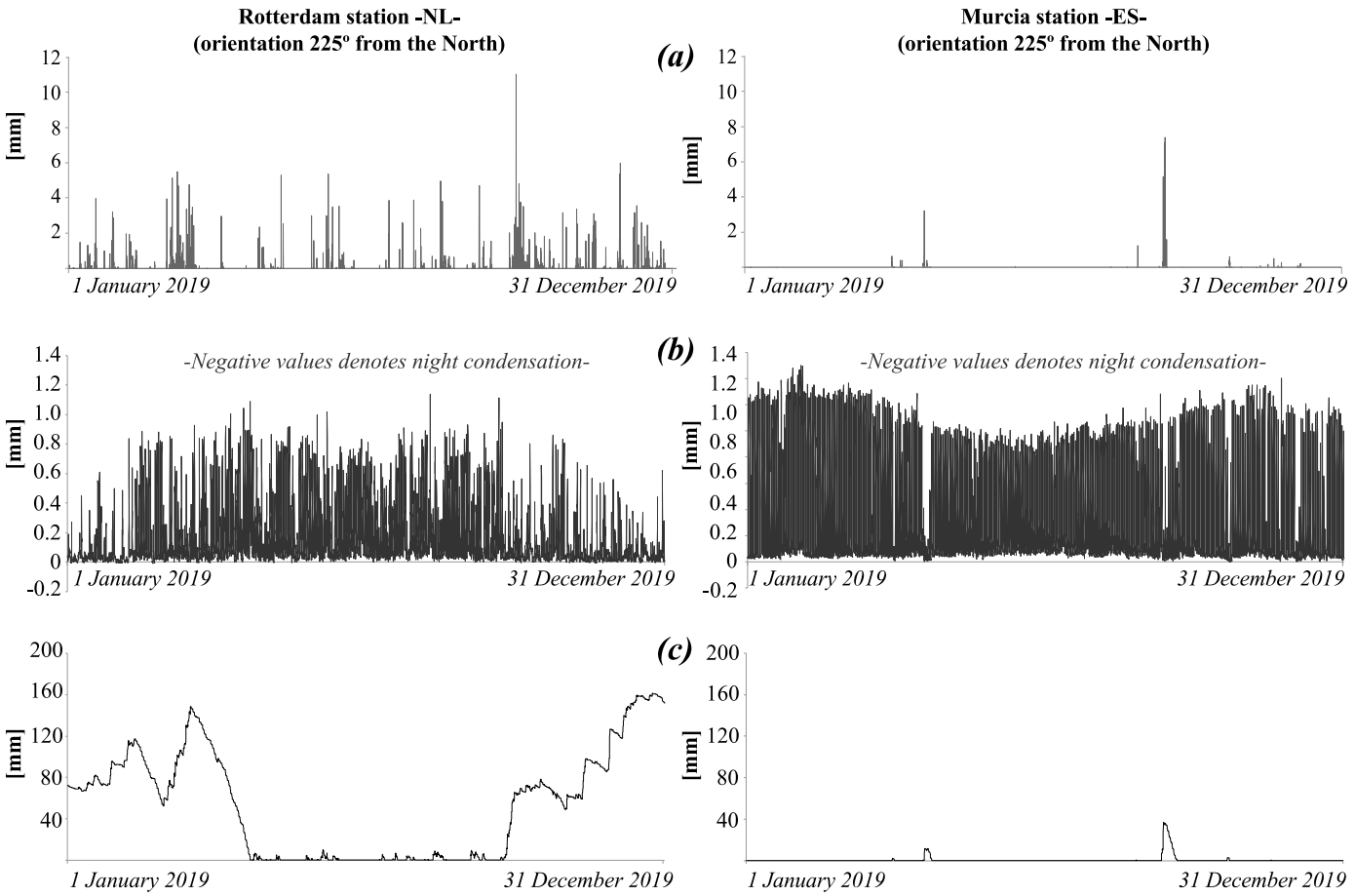

Fig. 5. Example of the proposed analysis of transient rainwater accumulated over time (January 1, 2019 to December 31, 2019), on the most exposed façades in Rotterdam and Murcia: *(a)* hourly WDR load; *(b)* hourly potential evaporation loss; *(c)* representative characterisation of potential rainwater content of the façade.

Table 1
Summary of the mean representative parameters involved in the proposed analysis.

Eindhoven station -NL-	*0°*	*45°*	*90°*	*135°*	*180°*	*225°*	*270°*	*315°*
Hours with WDR exposure (*h/yr*)	221.9	170.2	229.1	471.5	723.9	769.7	748.0	468.4
WDR load (*mm/yr*)	110.3	75.3	79.5	172.7	376.2	494.8	406.9	216.1
Potential evaporation E (*mm/yr*)	669.1	763.5	938.4	1092.6	1137.9	1082.4	933.2	766.8
Twente station -NL-	***0°***	***45°***	***90°***	***135°***	***180°***	***225°***	***270°***	***315°***
Hours with WDR exposure (*h/yr*)	243.8	187.1	238.4	528.8	736.8	785.1	775.5	443.4
WDR load (*mm/yr*)	106.7	78.0	77.0	167.2	374.2	494.3	398.1	205.2
Potential evaporation E (*mm/yr*)	608.4	701.6	869.2	1012.5	1045.9	988.9	850.0	697.7
Rotterdam station -NL-	***0°***	***45°***	***90°***	***135°***	***180°***	***225°***	***270°***	***315°***
Hours with WDR exposure (*h/yr*)	329.9	250.7	283.8	519.7	744.3	813.1	825.0	544.1
WDR load (*mm/yr*)	151.6	105.6	115.6	265.2	528.6	664.4	528.9	290.9
Potential evaporation E (*mm/yr*)	653.5	740.0	901.1	1052.3	1115.4	1086.2	944.1	764.9
Pozo de la Higuera station -ES-	***0°***	***45°***	***90°***	***135°***	***180°***	***225°***	***270°***	***315°***
Hours with WDR exposure (*h/yr*)	141.8	152.9	158.6	80.0	51.5	40.3	34.7	113.3
WDR load (*mm/yr*)	96.3	103.2	64.1	33.4	26.4	17.1	12.3	46.1
Potential evaporation E (*mm/yr*)	1126.8	1750.6	2496.3	2721.3	2804.5	2670.2	2260.3	1606.3
Murcia station -ES-	***0°***	***45°***	***90°***	***135°***	***180°***	***225°***	***270°***	***315°***
Hours with WDR exposure (*h/yr*)	69.8	69.8	79.7	173.1	161.7	161.7	151.8	58.4
WDR load (*mm/yr*)	14.0	23.3	24.8	27.9	38.7	37.6	20.4	7.3
Potential evaporation E (*mm/yr*)	1027.5	1563.7	2255.8	2645.9	2680.0	2654.5	2273.2	1581.6
Moratalla station -ES-	***0°***	***45°***	***90°***	***135°***	***180°***	***225°***	***270°***	***315°***
Hours with WDR exposure (*h/yr*)	151.8	128.6	112.6	118.3	125.6	148.6	164.6	159.1
WDR load (*mm/yr*)	69.3	50.8	41.9	41.3	42.1	60.4	82.8	89.4
Potential evaporation E (*mm/yr*)	1138.1	1744.1	2474.3	2702.1	2808.7	2679.9	2266.5	1615.1

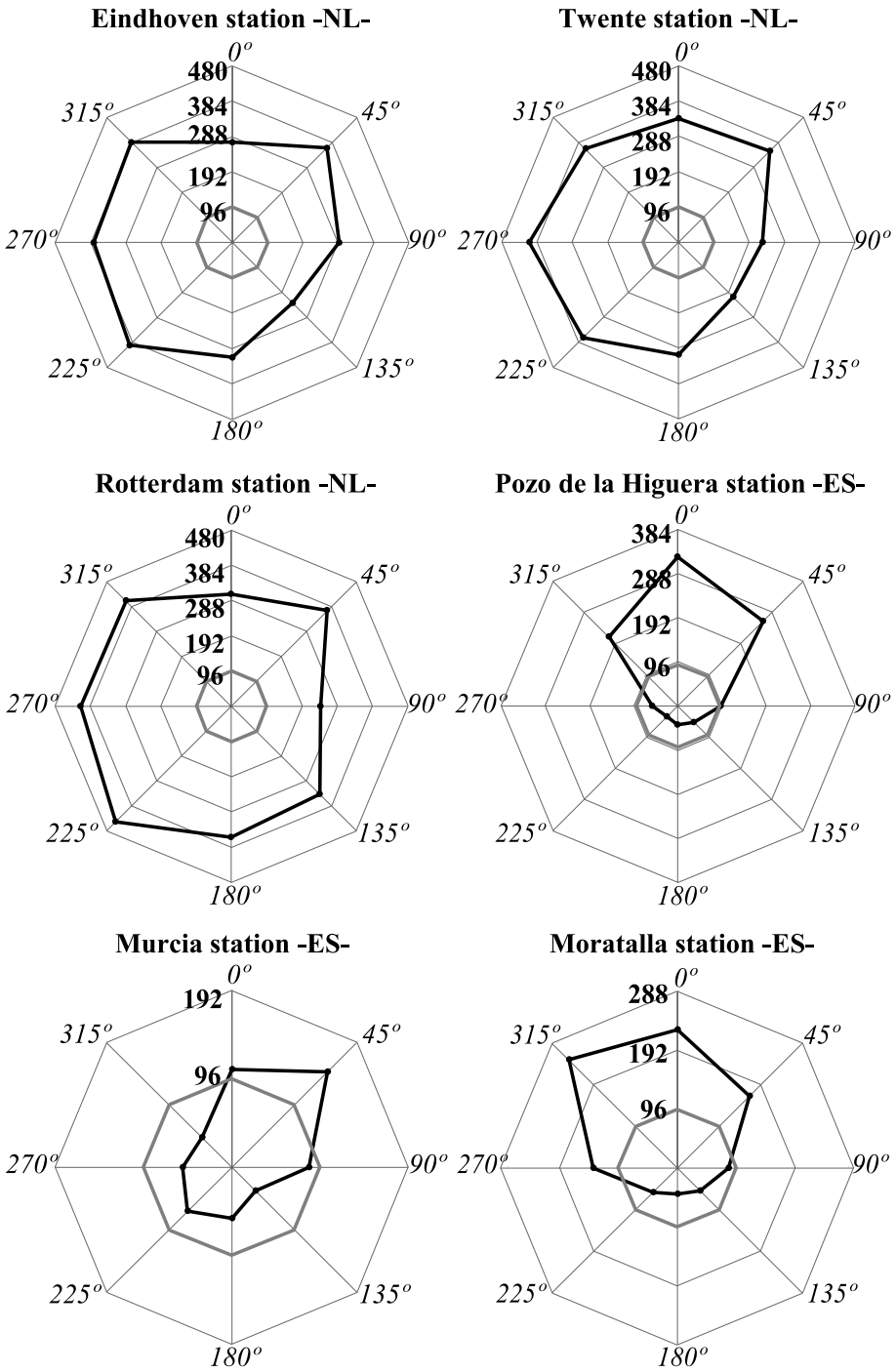

Fig. 6. Representative drying intervals (hours) associated with a three-year occurrence for each façade orientation in the analysed stations (degrees from North).

January 1, 2010 to December 31, 2019) (Royal Netherlands Meteorological Institute (KNMI), 2022; Agrarian information system of Murcia, 2022). Less than 10% of the hourly intervals lack records, which ensured the representativeness of the study (some characteristic data of these weather stations are summarised in Fig. 4). In turn, the analysis of records from 10 years prevented the results from being affected by periods of exceptional climatology.

In the absence of hourly records of atmospheric pressure at these weather stations, the value P (kPa) was estimated from the site elevation above sea level z (m) using the general gas equation (Eq. 27) (Allen et al., 1998; Walter et al., 2005).

$$P = 101.325 \cdot \left[(1 - 0.0000225577 \cdot z)^{5.25592} \right] \quad (27)$$

To estimate the surface temperature of the façades as well as their heat flux (see Eqs. (25) and (26)), the minimum R-values for the building façades fixed in both countries were considered. In The Netherlands, the minimum R-value for building façades in residential areas was set, in general, as 3.50 m^2 K/W (The Netherlands central government). In Spain, this minimum value depends on the climatic zone of each site, being equal to 2.04 m^2 K/W at Pozo de la Higuera and Murcia stations and equal to 2.44 m^2 K/W at Moratalla station (Spanish Ministry of Development, 2022).

Table 2
Representative drying intervals at each façade orientation and comparison of the episodic WDR exposures ($I_{S\theta}$ values) characterised from them and based on the 96-h ISO model.

Eindhoven station -NL-	***0º***	***45º***	***90º***	***135º***	***180º***	***225º***	***270º***	***315º***
Representative drying interval for a three-year occurrence *(h)*	272	365	290	231	311	393	375	386
I_s *(mm/spell);* from the façade-specific drying intervals	54.2	48.5	36.6	95.6	301.5	565.6	517.2	258.4
I_s *(mm/spell);* from the current 96-hour ISO model	29.8	21.8	23.8	38.4	109.9	139.7	113.6	54.0
Variation regarding ISO model (%)	*81.9*	*122.5*	*53.8*	*149.0*	*174.3*	*304.9*	*270.2*	*378.5*
Twente station -NL-	***0º***	***45º***	***90º***	***135º***	***180º***	***225º***	***270º***	***315º***
Representative drying interval for a three-year occurrence *(h)*	336	351	228	211	306	367	406	358
I_s *(mm/spell);* from the façade-specific drying intervals	76.7	57.0	30.0	103.3	339.9	630.6	604.2	231.2
I_s *(mm/spell);* from the current 96-hour ISO model	31.4	25.6	23.4	46.3	121.1	154.7	122.3	52.0
Variation regarding ISO model (%)	*144.3*	*122.7*	*28.2*	*123.1*	*180.7*	*307.6*	*394.0*	*344.6*
Rotterdam station -NL-	***0º***	***45º***	***90º***	***135º***	***180º***	***225º***	***270º***	***315º***
Representative drying interval for a three-year occurrence *(h)*	304	368	243	338	357	445	411	406
I_s *(mm/spell);* from the façade-specific drying intervals	76.5	67.8	52.5	200.5	547.2	914.4	769.8	354.1
I_s *(mm/spell);* from the current 96-hour ISO model	30.7	29.3	33.2	94.9	209.5	236.9	168.0	84.2
Variation regarding ISO model (%)	*149.2*	*131.4*	*58.1*	*111.3*	*161.2*	*286.0*	*358.2*	*320.5*
Pozo de la Higuera station -ES-	***0º***	***45º***	***90º***	***135º***	***180º***	***225º***	***270º***	***315º***
Representative drying interval for a three-year occurrence *(h)*	324	261	92	49	41	33	55	211
I_s *(mm/spell);* from the façade-specific drying intervals	65.2	63.0	34.9	15.0	11.5	6.7	9.7	26.4
I_s *(mm/spell);* from the current 96-hour ISO model	50.8	56.3	34.9	15.4	11.9	6.7	9.8	24.7
Variation regarding ISO model (%)	*28.3*	*11.9*	*0.0*	*-2.6*	*-3.4*	*0.0*	*-1.0*	*6.9*
Murcia station -ES-	***0º***	***45º***	***90º***	***135º***	***180º***	***225º***	***270º***	***315º***
Representative drying interval for a three-year occurrence *(h)*	106	147	83	37	55	68	54	45
I_s *(mm/spell);* from the façade-specific drying intervals	9.3	17.3	16.9	13.2	20.0	20.4	10.7	3.9
I_s *(mm/spell);* from the current 96-hour ISO model	9.3	17.3	16.9	13.9	20.7	21.5	11.6	4.0
Variation regarding ISO model (%)	0.0	0.0	0.0	-5.0	-3.4	-5.1	-7.8	-2.5
Moratalla station -ES-	***0º***	***45º***	***90º***	***135º***	***180º***	***225º***	***270º***	***315º***
Representative drying interval for a three-year occurrence *(h)*	225	166	84	52	42	56	136	249
I_s *(mm/spell);* from the façade-specific drying intervals	28.1	19.8	17.5	15.8	11.2	21.6	36.1	39.1
I_s *(mm/spell);* from the current 96-hour ISO model	25.7	18.8	17.5	16.1	12.7	24.3	35.7	32.7
Variation regarding ISO model (%)	*9.3*	*5.3*	*0.0*	*-1.9*	*-11.8*	*-11.1*	*1.1*	*19.9*

4. Results and discussion

As stated above, various stochastic factors determine the amount of rainwater that can be evaporated at any given time. Furthermore, water absorption is material and time-dependent at the beginning of WDR exposure, transitioning into specific rainwater infiltrations once the outer surface becomes saturated (Hall and Hoff, 2012; Van Linden and Van Den Bossche, 2022; Beijer, 1977; Kahangi et al., 2021; Shahreza et al., 2022). Therefore, considering a specific value of WDR load to be evaporated would deviate the generic nature as intended in the ISO standard. A more reliable characterisation of the wetting conditions from exposure to WDR, regardless of the type of façade materials used, would be the straightforward comparison between the potential evaporative loss from the surface and all the coincident WDR load, for each façade orientation.

Such a characterisation would provide a useful tool to universally compare representative drying intervals and spell indices, in consideration of the specific environmental factors at each site. In this study, the characterisation was performed by discretising the possible façade orientations at 45° intervals, thus performing eight independent analyses for each location of interest. Given the analytical nature of the equations previously presented, the calculation was performed using conventional spreadsheets, with a total of 87,648 rows corresponding to the hourly intervals within the 10 years considered. However, nothing prevents the implementation of a more efficient type of automation for the calculation.

4.1. Transient wetting conditions on the façades

Fig. 5 presents an example of the variation of potential rainwater content over time (for clarity, only that of a single year is shown) obtained from the combination of 100% of WDR load and potential evaporation loss on the most exposed façade orientation of the location. The WDR exposures were mostly evenly distributed throughout the year in The Netherlands, whereas for the Spanish station locations only occasional WDR loads were identified, mainly in the form of very intense events of short duration concentrated in the autumn (due to the so-called cold drops).

As a result of the higher temperatures and greater solar radiation received by building façades, potential evaporation intensifies during the summer. On an hourly scale, potential evaporation increased during the day and decreased at night. On nights with propitious conditions (i.e. low temperature, high relative humidity, and without appreciable wind), the potential evaporation loss E (mm/h) can reach negative values, which reveals condensation on the façade as a result of overcooling (causing a slight increase in the water content). It should be noted that the potential evaporation losses were significantly higher at Spanish as compared to Dutch stations. In The Netherlands, diffuse radiation equalled and even exceeded the amount of direct radiation, which minimised the difference in potential evaporation loss between different façade orientations. In contrast, for all façades located at the Murcian sites in Spain, facing the Earth's equator and having a much greater contribution of direct radiation, the potential evaporation loss increased significantly (Table 1).

4.2. Duration of the evaporation intervals required to dry previous WDR loads

To define the drying interval of 96 h, the ISO standard only states that there may be periods of up to 96 consecutive hours without WDR before evaporation losses exceed rain gains, with no further clarification. In this study, the time intervals required to evaporate the prior

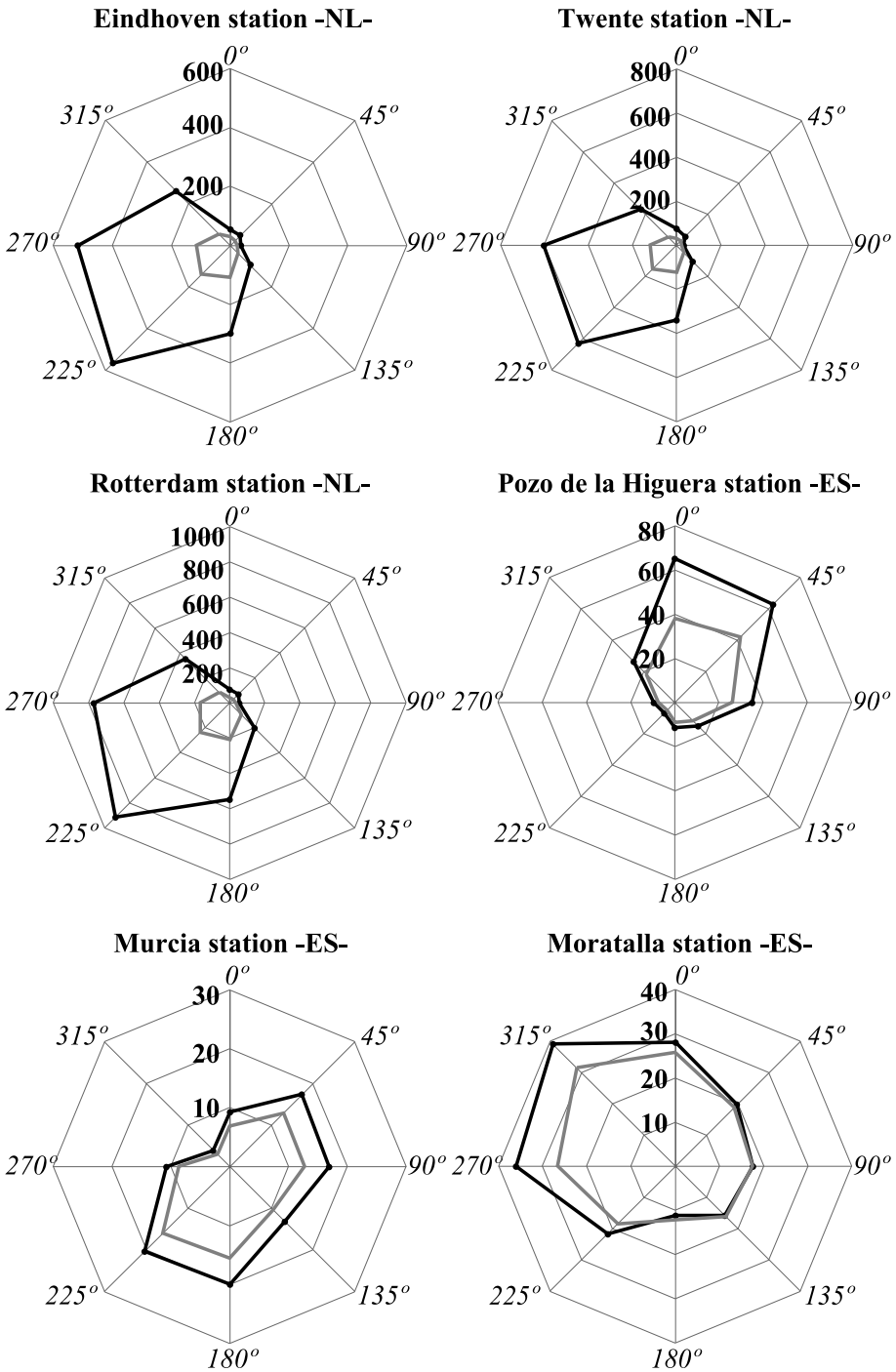

Fig. 7. Comparison of WDR spell indices for each façade orientation in the analysed stations (degrees from North).

WDR loads were analysed from the first WDR load of the spell until all water was evaporated. Thus, the number of hours elapsed between the last WDR load of the spell and final drying were counted. For consistency with the ISO standard, the computation was not restarted until a new WDR load affected the façade orientation, thus omitting any prior wetting caused by intermediate condensations (i.e. not attributable to WDR).

The longest drying interval that can occur with a three-year return period was maintained as the representative value for each façade orientation. This decision is consistent with the definition of the ISO spell index (i.e. the worst spell likely to occur in any three-year period), although the use of this particular return period is not clearly justified and could also be discussed. Fig. 6 shows the duration of these façade-specific drying intervals identified for the analysed façades and their comparison with the generic 96 h currently considered.

As expected, owing to the higher potential evaporation and lower WDR loads, Spanish stations showed shorter drying intervals than those identified in The Netherlands (see Table 2). For the Spanish stations, it was observed that the drying intervals were shorter on south-facing façades because of the greater amount of solar radiation received (Pozo de la Higuera, 33 h, 225°; Murcia, 37 h, 135°; Moratalla, 42 h, 180°). In turn, the north-facing façades present the most unfavourable

Table 3
Representative drying intervals identified by using values of external surface thermal resistance dependent on wind speed (Eq. (28)).

Eindhoven station -NL-	*Mean R_{se} value = 0.048* m^2 K/W	*0°*	*45°*	*90°*	*135°*	*180°*	*225°*	*270°*	*315°*	*Avg.*
Representative drying interval for a three-year occurrence *(h)*		277	372	291	238	311	397	375	387	
Percentage variation regarding constant R_{se} = 0.04 m^2 K/W		*1.8*	*1.9*	*0.3*	*3.0*	*0.0*	*0.8*	*0.0*	*0.3*	***1.0***
Twente station -NL-	*Mean R_{se} value = 0.051* m^2 K/W	***0°***	***45°***	***90°***	***135°***	***180°***	***225°***	***270°***	***315°***	
Representative drying interval for a three-year occurrence *(h)*		337	354	230	226	308	370	409	359	
Percentage variation regarding constant R_{se} = 0.04 m^2 K/W		*0.3*	*0.3*	*0.9*	*7.1*	*0.7*	*0.8*	*0.7*	*0.3*	***1.4***
Rotterdam station -NL-	*Mean R_{se} value = 0.045* m^2 K/W	***0°***	***45°***	***90°***	***135°***	***180°***	***225°***	***270°***	***315°***	
Representative drying interval for a three-year occurrence *(h)*		305	360	245	349	366	446	414	407	
Percentage variation regarding constant R_{se} = 0.04 m^2 K/W		*0.3*	*0.3*	*0.8*	*3.3*	*2.5*	*0.2*	*0.7*	*0.2*	***1.0***
Pozo de la Higuera station -ES-	*Mean R_{se} value = 0.059* m^2 K/W	***0°***	***45°***	***90°***	***135°***	***180°***	***225°***	***270°***	***315°***	
Representative drying interval for a three-year occurrence *(h)*		328	267	105	51	44	33	56	212	
Percentage variation regarding constant R_{se} = 0.04 m^2 K/W		*1.2*	*2.3*	*14.4*	*4.1*	*7.3*	*0.0*	*1.8*	*0.5*	***4.0***
Murcia station -ES-	*Mean R_{se} value = 0.082* m^2 K/W	***0°***	***45°***	***90°***	***135°***	***180°***	***225°***	***270°***	***315°***	
Representative drying interval for a three-year occurrence *(h)*		112	156	104	48	65	82	60	50	
Percentage variation regarding constant R_{se} = 0.04 m^2 K/W		5.7	6.1	25.3	29.7	18.2	20.6	11.1	11.1	**16.0**
Moratalla station -ES-	*Mean R_{se} value = 0.065* m^2 K/W	***0°***	***45°***	***90°***	***135°***	***180°***	***225°***	***270°***	***315°***	
Representative drying interval for a three-year occurrence *(h)*		228	177	89	56	44	61	144	253	
Percentage variation regarding constant R_{se} = 0.04 m^2 K/W		*1.3*	*6.6*	*6.0*	*7.7*	*4.8*	*8.9*	*5.9*	*1.6*	***5.4***

intervals, reaching 324 h (0°), 249 h (315°), and 147 h (45°) for Pozo de la Higuera, Moratalla and Murcia stations, respectively. It should be noted that in most of the façades located in Spain the required drying intervals were shorter than 96 h as established in the ISO standard, even considering the evaporation of all the WDR load as had been deposited on the façade. In the Netherlands, these representative drying intervals range between 211 h and 406 h at the Twente station (135° and 270°, respectively), whereas for the remaining Dutch stations the intervals are quite similar: from 231 h (135°) to 393 h (225°) for Eindhoven and between 243 h (90°) and 445 h (225°) for Rotterdam.

As demonstrated, the required drying intervals vary significantly with respect to façade orientation and location. Specifically, this variation reaches 291 h between the façade orientations of Pozo de la Higuera as well as 207 h in Moratalla, 202 h in Rotterdam, and 19 h in Twente. Considering the six weather stations analysed, the maximum variation reaches 412 h between Pozo de la Higuera (225°) and Rotterdam (225°). Consequently, considering a constant drying interval of 96 h entails an indeterminate uncertainty in the spell indices as characterised in the current ISO standard.

4.3. Comparison of spell indices: 96-h ISO 15927-3 model versus façade-specific spell approach

Considering the specific drying intervals identified for each façade orientation, improved WDR spell indices were calculated using a method analogous to that established in the current ISO standard. Thus, each of these façade-specific spells was limited by the occurrence of a number of hours without WDR, which depends directly on the local climate factors to which each façade is (Fig. 6). Once the $I'_{S\theta}$ values associated with these façade-specific spells are obtained, improved spell indices ($I_{S\theta}$ values) being more representative of local conditions can be calculated. In Fig. 7, the improved spell indices are compared with those obtained using the conventional ISO calculation (i.e. considering 96 h without WDR as a limitation for each spell).

Values of both the ISO and improved indices are summarised in Table 2, as well as their percentage variation. In general, increased episodic WDR exposures were estimated using the proposed method compared to that provided by the 96-h ISO model, owing to consideration of the entire WDR load as evaporable rainwater. Some façade orientations in The Netherlands present WDR spells that last more than a year, causing spell indices to exceed the mean annual WDR exposure. The greatest differences (absolute and in percentage) were indeed identified in locations with higher WDR exposure, due to consideration of longer WDR spells than those of the ISO standard (+378.5% in Eindhoven, +394.0% in Twente, and +358.2% in Rotterdam). In the Region of Murcia, considering drying intervals different than the 96 h of the ISO standard causes a much smaller effect on the spell index, given the fewer and more occasional precipitation events.

It should be noted that the greater intensity and more continuous the exposure event to WDR the more sensitive the values for spell index are to the drying interval duration. As a result, the uncertainty of the 96-h ISO model is greater the more unfavourable the WDR exposure of the location: variations ranging from +28.2% to +394.0% can be identified with regard to ISO spell indices for different façade orientations at Twente station. Even so, the results demonstrate that the 96-h ISO model reasonably characterises the façade orientations subjected to the most unfavourable spell indices (shaded values in Table 2).

4.4. Sensitivity of method results and their comparison with the 96-h ISO model when adjusted for generic brick walls

The proposed mathematical framework incorporates models to determine the diffuse radiation present in measured radiation records (Erbs et al.), to quantify the influence of each radiative component (Hay), and to estimate the effective atmospheric emissivity with cloudiness (Berdahl and Martin), among others. Despite this, other alternative models could be used to provide a more accurate representation of specific atmospheric conditions. In turn, various simplifications have allowed decoupling the results from the nature of façade materials, as well as achieving a more functional calculation.

An example of a possible improvement for these simplifications would be to consider the effect of wind speed on the external surface

Table 4
Representative drying intervals identified by using different albedo values for façade materials.

Eindhoven station -NL-	*0°*	*45°*	*90°*	*135°*	*180°*	*225°*	*270°*	*315°*	*Avg.*
Drying interval considering albedo ρ = 0.1 *(h)*	269	364	280	203	293	381	371	385	
Percentage variation regarding ρ = 0.2	*−1.1*	*−0.3*	*−3.4*	*−12.1*	*−5.8*	*−3.1*	*−1.1*	*−0.3*	***−3.4***
Drying interval considering albedo ρ = 0.4 *(h)*	293	379	305	266	344	410	375	393	
Percentage variation regarding ρ = 0.2	*7.7*	*3.8*	*5.2*	*15.2*	*10.6*	*4.3*	*0.0*	*1.8*	***6.1***

Twente station -NL-	***0°***	***45°***	***90°***	***135°***	***180°***	***225°***	***270°***	***315°***	
Drying interval considering albedo ρ = 0.1 *(h)*	334	349	226	196	304	356	396	357	
Percentage variation regarding ρ = 0.2	*−0.6*	*−0.6*	*−0.9*	*−7.1*	*−0.7*	*−3.0*	*−2.5*	*−0.3*	***−2.0***
Drying interval considering albedo ρ = 0.4 *(h)*	341	359	241	262	334	372	447	374	
Percentage variation regarding ρ = 0.2	*1.5*	*2.3*	*5.7*	*24.2*	*9.2*	*1.4*	*10.1*	*4.5*	***7.4***

Rotterdam station -NL-	***0°***	***45°***	***90°***	***135°***	***180°***	***225°***	***270°***	***315°***	
Drying interval considering albedo ρ = 0.1 *(h)*	303	367	241	325	350	431	409	404	
Percentage variation regarding ρ = 0.2	*−0.3*	*−0.3*	*−0.8*	*−3.8*	*−2.0*	*−3.1*	*−0.5*	*−0.5*	***−1.4***
Drying interval considering albedo ρ = 0.4 *(h)*	309	373	247	372	378	468	436	422	
Percentage variation regarding ρ = 0.2	*1.6*	*1.4*	*1.6*	*10.1*	*5.9*	*5.2*	*6.1*	*3.9*	***4.5***

Pozo de la Higuera station -ES-	***0°***	***45°***	***90°***	***135°***	***180°***	***225°***	***270°***	***315°***	
Drying interval considering albedo ρ = 0.1 *(h)*	323	253	85	48	40	33	54	211	
Percentage variation regarding ρ = 0.2	*−0.3*	*−3.1*	*−7.6*	*−2.0*	*−2.4*	*0.0*	*−1.8*	*0.0*	***−2.2***
Drying interval considering albedo ρ = 0.4 *(h)*	330	285	117	55	45	37	61	214	
Percentage variation regarding ρ = 0.2	*1.9*	*9.2*	*27.2*	*12.2*	*9.8*	*12.1*	*10.9*	*1.4*	***10.6***

Murcia station -ES-	***0°***	***45°***	***90°***	***135°***	***180°***	***225°***	***270°***	***315°***	
Drying interval considering albedo ρ = 0.1 *(h)*	105	145	81	36	54	65	50	45	
Percentage variation regarding ρ = 0.2	*−0.9*	*−1.4*	*−2.4*	*−2.7*	*−1.8*	*−4.4*	*−7.4*	*0.0*	***−2.6***
Drying interval considering albedo ρ = 0.4 *(h)*	110	155	98	44	64	79	59	49	
Percentage variation regarding ρ = 0.2	*3.8*	*5.4*	*18.1*	*18.9*	*16.4*	*16.2*	*9.3*	*8.9*	***12.1***

Moratalla station -ES-	***0°***	***45°***	***90°***	***135°***	***180°***	***225°***	***270°***	***315°***	
Drying interval considering albedo ρ = 0.1 *(h)*	224	162	82	51	42	53	129	246	
Percentage variation regarding ρ = 0.2	*−0.4*	*−2.4*	*−2.4*	*−1.9*	*0.0*	*−5.4*	*−5.1*	*−1.2*	***−2.4***
Drying interval considering albedo ρ = 0.4 *(h)*	230	179	89	56	45	65	148	255	
Percentage variation regarding ρ = 0.2	*2.2*	*7.8*	*6.0*	*7.7*	*7.1*	*16.1*	*8.8*	*2.4*	***7.3***

thermal resistance R_{se} (m^2·K/W), instead of adopting a constant value (refer to Eq. (25)). Although there is a wide variety of models for this purpose, the one suggested in ISO standard 6946 would not involve additional calculation effort (Eq. (28)). In this equation, U_{10} (m/s) represents the wind speed near the façade at a reference height of 10 m, $\varepsilon_{façade}$ (−) is the emissivity of the façade material, previously established as 0.910, σ expresses the Stefan–Boltzmann constant ($5.67{\cdot}10^{-8}$ W/m^2·K^4), and T (K) could be assimilated to the external air temperature:

$$R_{se} = \frac{1}{4 + 4{\cdot}U_{10} + 4{\cdot}\varepsilon_{façade}{\cdot}\sigma{\cdot}T^{3}} \tag{28}$$

The variations induced in the duration of representative drying intervals, considering the refined R_{se} value associated with each hourly wind record, are shown in Table 3. As observed, the mean R_{se} values identified are consistently higher than the established constant value (0.04 m^2 K/W), ranging from 0.045 in Rotterdam station to 0.082 m^2 K/W in Murcia station. Variations in drying intervals are more pronounced in the Spanish stations (characterised by higher R_{se} values), reaching a mean value of 16.0% in Murcia station. Nevertheless, the sensitivity of the method to this parameter remains below 7.1% in all Dutch façades (Twente station, 315°). This calculation illustrates one of the numerous possibilities of incorporating refined models into the proposed method, provided they continue to allow the general comparison of obtained drying intervals for different locations and façade types.

Another factor under discussion could be the albedo value (0.2) considered for façades (see Eqs. (22) and (25)). In general, the median albedo in urbanised surroundings vary between 0.11 and 0.34, within a range of typical scenarios (Oke, 1987; Krayenhoff and Voogt, 2010; Trlica et al., 2017). To quantify the influence of this parameter in the calculation, previous results have been compared with those obtained by fixing other representative albedo values close to that range (Table 4). As can be seen, a lower albedo (ρ = 0.1) increases the absorption of radiation by the façade and favours the evaporation process: the representative drying intervals are moderately shortened, especially on façades facing south (e.g., Eindhoven, −12.1%, 135°; Pozo de la Higuera, −7.6%, 90°; Twente, −7.1%, 135°). If the albedo is doubled (ρ = 0.4), the net radiation absorbed by the façade is reduced, decreasing the available energy for evaporation and lengthening the representative drying intervals (Pozo de la Higuera, +27.2%, 90°; Twente, +24.2%, 135°; Murcia, +18.9%, 135°).

To illustrate the sensitivity of the method to wind speed, the calculation of representative drying intervals for each façade orientation was conducted by arbitrarily weighting the available wind records at the stations (x0.5 and x1.5). For this analysis, the actual value of the incident WDR load was maintained, allowing to distinguish the influence of wind speed on the evaporative potential of the façades. As shown in Table 5, a lower wind speed reduces the aerodynamic component of potential evaporation, thus extending the drying intervals, and vice versa. In general, south-facing façades show minor variations due to the greater influence of the radiation component on the duration of drying intervals. For this reason, overall, the drying intervals of Dutch façades

Table 5
Representative drying intervals identified by using increased (x1.5) and decreased (x0.5) values of wind speed, while maintaining the actual WDR load.

Eindhoven station -NL-	*0°*	*45°*	*90°*	*135°*	*180°*	*225°*	*270°*	*315°*	*Avg.*
Drying intervals with 0.5·U_{10} and equal WDR load *(h)*	337	410	349	273	352	410	383	434	
Percentage variation regarding actual drying intervals	*23.9*	*12.3*	*20.3*	*18.2*	*13.2*	*4.3*	*2.1*	*12.4*	***13.3***
Drying intervals with 1.5·U_{10} and equal WDR load *(h)*	247	279	248	185	270	356	367	314	
Percentage variation regarding actual drying intervals	*−9.2*	*−23.6*	*−14.5*	*−19.9*	*−13.2*	*−9.4*	*−2.1*	*−18.7*	***−13.8***
Twente station -NL-	***0°***	***45°***	***90°***	***135°***	***180°***	***225°***	***270°***	***315°***	
Drying intervals with 0.5·U_{10} and equal WDR load *(h)*	339	397	295	276	328	373	468	447	
Percentage variation regarding actual drying intervals	*0.9*	*13.1*	*29.4*	*30.8*	*7.2*	*1.6*	*15.3*	*24.9*	***15.4***
Drying intervals with 1.5·U_{10} and equal WDR load *(h)*	286	314	210	185	297	320	352	313	
Percentage variation regarding actual drying intervals	*−14.9*	*−10.5*	*−7.9*	*−12.3*	*−2.9*	*−12.8*	*−13.3*	*−12.6*	***−10.9***
Rotterdam station -NL-	***0°***	***45°***	***90°***	***135°***	***180°***	***225°***	***270°***	***315°***	
Drying intervals with 0.5·U_{10} and equal WDR load *(h)*	382	425	314	379	381	469	443	435	
Percentage variation regarding actual drying intervals	*25.7*	*15.5*	*29.2*	*12.1*	*6.7*	*5.4*	*7.8*	*7.1*	***13.7***
Drying intervals with 1.5·U_{10} and equal WDR load *(h)*	240	243	227	278	348	404	354	305	
Percentage variation regarding actual drying intervals	*−21.1*	*−34.0*	*−38.3*	*−17.8*	*−2.5*	*−9.2*	*−13.9*	*−24.9*	***−20.2***
Pozo de la Higuera station -ES-	***0°***	***45°***	***90°***	***135°***	***180°***	***225°***	***270°***	***315°***	
Drying intervals with 0.5·U_{10} and equal WDR load *(h)*	347	302	101	53	45	37	58	238	
Percentage variation regarding actual drying intervals	*7.1*	*15.7*	*9.8*	*8.2*	*9.8*	*12.1*	*5.5*	*12.8*	***10.1***
Drying intervals with 1.5·U_{10} and equal WDR load *(h)*	278	219	87	48	40	32	48	192	
Percentage variation regarding actual drying intervals	*−14.2*	*−16.1*	*−5.4*	*−2.0*	*−2.4*	*−3.0*	*−12.7*	*−9.0*	***−8.1***
Murcia station -ES-	***0°***	***45°***	***90°***	***135°***	***180°***	***225°***	***270°***	***315°***	
Drying intervals with 0.5·U_{10} and equal WDR load *(h)*	116	155	89	38	56	72	56	51	
Percentage variation regarding actual drying intervals	*9.4*	*5.4*	*7.2*	*2.7*	*1.8*	*5.9*	*3.7*	*13.3*	***6.2***
Drying intervals with 1.5·U_{10} and equal WDR load *(h)*	95	140	80	35	54	62	46	41	
Percentage variation regarding actual drying intervals	*−10.4*	*−4.8*	*−3.6*	*−5.4*	*−1.8*	*−8.8*	*−14.8*	*−8.9*	***−7.3***
Moratalla station -ES-	***0°***	***45°***	***90°***	***135°***	***180°***	***225°***	***270°***	***315°***	
Drying intervals with 0.5·U_{10} and equal WDR load *(h)*	246	181	87	54	47	63	147	274	
Percentage variation regarding actual drying intervals	*9.3*	*9.0*	*3.6*	*3.8*	*11.9*	*12.5*	*8.1*	*10.0*	***8.5***
Drying intervals with 1.5·U_{10} and equal WDR load *(h)*	210	150	82	51	41	51	125	221	
Percentage variation regarding actual drying intervals	*−6.7*	*−9.6*	*−2.4*	*−1.9*	*−2.4*	*−8.9*	*−8.1*	*−11.2*	***−6.4***

Table 6
Representative drying intervals (hours) identified by evaporating a part of the incident WDR load, characteristic for generic brick walls (*shaded values denote the maximum drying intervals)*.

Eindhoven station -NL-	***0°***	***45°***	***90°***	***135°***	***180°***	***225°***	***270°***	***315°***	***Avg.***
Drying interval to evaporate 1% of WDR load *(h)*	22	19	24	25	25	24	23	23	***23***
Drying interval to evaporate 10% of WDR load *(h)*	56	70	68	52	54	75	72	54	***63***
Drying interval to evaporate 20% of WDR load *(h)*	126	126	109	84	91	112	128	92	***109***
Twente station -NL-	***0°***	***45°***	***90°***	***135°***	***180°***	***225°***	***270°***	***315°***	
Drying interval to evaporate 1% of WDR load *(h)*	37	33	38	46	46	46	43	32	***40***
Drying interval to evaporate 10% of WDR load *(h)*	76	85	54	81	66	68	72	84	***73***
Drying interval to evaporate 20% of WDR load *(h)*	129	152	86	86	79	128	149	119	***115***
Rotterdam station -NL-	***0°***	***45°***	***90°***	***135°***	***180°***	***225°***	***270°***	***315°***	
Drying interval to evaporate 1% of WDR load *(h)*	23	26	26	30	26	22	19	20	***24***
Drying interval to evaporate 10% of WDR load *(h)*	44	51	46	51	59	83	65	54	***57***
Drying interval to evaporate 20% of WDR load *(h)*	79	77	80	74	96	116	115	121	***95***

are more affected than those of Spanish façades. As a result, the greatest reductions are identified in Rotterdam (−38.3%; 90°) and Eindhoven (−23.6%; 45°). In turn, the greatest extensions of representative drying intervals are observed in Twente (+30.8%; 135°) and Rotterdam (+29.2%; 90°).

In any case, the main factor influencing the duration of drying intervals is the amount of WDR load considered for evaporation. Initially, 100% of the hourly WDR load has been considered to avoid the complex interaction of material nature and to provide representative values comparable everywhere and for any façade type. Nevertheless, it is also possible to perform an adjusted calculation by considering only a portion of this WDR exposure. This approach can be used to estimate the behaviour of specific façade types, such as the brick walls used to establish the 96-h ISO model.

Considering the exterior surface of the material is saturated and the rainwater flow through the outer layer has already been established as the most unfavourable situation, brick walls can reach infiltration rates ranging from 0.22% to 47.04% of the incident WDR load, depending on their components, workmanship, test conditions, etc. (Van Linden and Van Den Bossche, 2022; Van Den Bossche et al., 2011). However, in general, most experimental studies consider a range between 0 and 20% (Shahreza et al., 2022), while ASHRAE standard 160 establishes the penetration of 1% of the rain incident on the cladding, in the absence of better data (ASHRAE Standard 160, 2016).

Table 6 presents the representative drying intervals identified by estimating the evaporation of 1%, 10% and 20% of the WDR load impinging on the analysed Dutch façades. Assuming that their climate shares certain similarities with that of the United Kingdom (Spanish stations are excluded in this case), these conditions would approximately recreate those that could have occurred when the drying period of 96 h was established for brick walls.

Considering the inherent climatic differences and the lack of details regarding the tests conducted in the United Kingdom over half a century ago, the results from the three stations show a reasonable convergence with the 96-h ISO model within the typical infiltration rates identified for this type of façades. As observed, the approximation is particularly suitable for infiltration rates close to 20%, with maximum drying intervals and average values around 96 h. Even when considering the evaporation of these reduced portions of WDR load, variations between locations and façade orientations can be significant, thus demonstrating the utility of the proposed method in providing a generic and representative consideration of local and orientation factors influencing façade drying durations.

All these results suggest that the current ISO standard to minimise uncertainties when characterising WDR spell indices in varied regions and façade orientations be revised, for which the proposed procedure represents an analytical and adaptable alternative for functional implementation. The proposed analysis allows reassessing the value of the spell indices currently identified, considering the climatic conditions of each region and the façade orientations while preserving the generic nature of the ISO standard. It would be advisable to analyse various locations within each region to create maps that, suitable for inclusion in the ISO standard 15927-3, show a representative duration of drying intervals to be considered at each site, thus replacing the current 96 h. In turn, it is expected that this improved approach will open new paths for the refinement of the proposed formulation, as well as for consideration of rainwater absorption rates adjusted to specific façade materials. In this regard, a future empirical validation of these non-generic adjustments would be useful.

5. Conclusions

The improvement of international standards is a task of great interest because of their widespread use. Our study has demonstrated the need to reconsider the simplistic spell definition given in ISO standard 15927-3 by including local environmental factors that affect the wetting conditions of building façades over time. At present, the generic drying interval of 96 h set in the ISO standard is methodologically weak and can cause façade designs to potentially be unsuitable for resistance to WDR events.

Variations of up to 291 h were identified between the representative drying intervals on different façade orientations (Pozo de la Higuera, Spain). In turn, variations of up to 412 h were also found between different locations (Pozo de la Higuera -Spain- and Rotterdam -The Netherlands-). These variations can cause significant uncertainties when characterising spell indices based on the 96-h ISO model, which were more noticeable with higher the WDR exposure.

The proposed methodological change (replacing the simplistic interval of 96 h with façade-specific drying intervals that consider the main local factors driving water evaporation on façade surfaces) can constitute a key improvement to minimise the uncertainty of generic spell indices. This provides a more reliable estimate of episodic WDR exposures, while achieving their comparability across geographic regions regardless of the façade materials. Although the proposed formulation admits multiple adjustments, this novel approach enables functional estimation of the drying intervals required to evaporate previous WDR loads, on the basis of weather records usually available together with those used by the current 96-h ISO model.

CRediT authorship contribution statement

José M. Pérez-Bella: Writing – original draft, Validation, Methodology, Funding acquisition, Conceptualization. **Javier Domínguez-Hernández:** Writing – review and editing, Formal analysis, Conceptualization. **Elena Ibarz-Montaner:** Validation, Investigation. **Martín Orna-Carmona:** Visualization, Data curation. **Ángel Salesa-Bordanaba:** Software, Resources. **Scott A. Orr:** Writing – review and editing, Supervision.

Declaration of Generative AI and AI-assisted technologies in the writing process

During the preparation of this work the authors did not used Generative AI. The authors reviewed and edited the content as needed and take full responsibility for the content of the publication. Readability and language was improved by Elsevier Language Editing Services.

Declaration of competing interest

The authors declare that they have no known competing financial interests or personal relationships that could have appeared to influence the work reported in this paper.

Data availability

Data will be made available on request.

Acknowledgements

Project *PID 2021-122203OB-I00* funded by MCIN/AEI/10.13039/501100011033 and by ERDF A way of making Europe. The authors acknowledge the help provided by engineer Alicia C. Casas Aguirre with the data processing as well as the collaboration of doctor in geological science Pedro L. López Julián.

References

Abuku, M., Janssen, H., Roels, S., 2009. Impact of wind-driven rain on historic brick wall buildings in a moderately cold and humid climate: numerical analyses of mould growth risk, indoor climate and energy consumption. Energy Build. 41–1, 101–110. https://doi.org/10.1016/j.enbuild.2008.07.011.

Agrarian information system of Murcia, 2022. Government of the Region of Murcia, Personalised Agrometeorological Report (in Spanish). http://siam.imida.es/apex/f?p=101:46:913350602421486. (Accessed 27 July 2023).

Algarni, S., Nutter, D., 2015. Survey of sky effective temperature models applicable to building envelope radiant heat transfer. Ashrae Tran 121 (2), 351–363. https://doi.org/10.13140/RG.2.1.4212.5526.

Allen, R.G., Pereira, L.S., Raes, D., Smith, M., 1998. Crop Evapotranspiration (Guidelines for Computing Crop Water Requirements) - FAO Irrigation and Drainage Paper No. 56. FAO - Food and Agriculture Organization of the United Nations, Rome.

An, N., Hemmati, S., Cui, Y., 2017. Assessment of the methods for determining net radiation at different time-scales of meteorological variable. J. Rock Mech. Geotech. Eng. 9, 239–246. https://doi.org/10.1061/j.jrmge.2016.10.004.

Arce, M., García, S., Van den Bossche, N., 2017. Experimental assessment of rainwater management of a ventilated façade. J. Build. Phys. 42 (1), 38–67. https://doi.org/10.1177/1744259117719077.

ASHRAE Standard 160, Criteria for Moisture Control Design Analysis in Buildings, 2016. American Society of Heating, Refrigerating and Air-Conditioning Engineers, Atlanta.

Bastien, D., Winther-Gaasvig, M., 2018. Influence of driving rain and vapour diffusion on the hygrothermal performance of a hygroscopic and permeable building envelope. Energy 164, 288–297. https://doi.org/10.1016/j.energy.2018.07.195.
Beijer, O., 1977. Concrete walls and weathering. In: Presented at the RILEM/ASTM/CIB Symposium on Evaluation of the Performance of External Vertical Surfaces on Buildings.
Berdahl, P., Martin, M., 1984. Emissivity of clear skies. Sol. Energy 32:5, 663–664. https://doi.org/10.1016/0038-092X(84)90144-0.
Blender Online Community, Blender - a 3D Modelling and Rendering Package, 2023. Stichting Blender Foundation. http://www.blender.org. (Accessed 12 November 2023).
Blocken, B., Carmeliet, J., 2004. A review of wind-driven rain research in building science. J. Wind Eng. Ind. Aerod. 92–13, 1079–1130. https://doi.org/10.1016/j.jweia.2004.06.003.
Blocken, B., Derome, D., Carmeliet, J., 2013. Rainwater runoff from building facades: a review. Build. Environ. 60, 339–361. https://doi.org/10.1016/j.buildenv.2012.10.008.
Building Energy and Environmental Systems Laboratory, 2006. Department of Mechanical and Aerospace Engineering; Syracuse University, CHAMPS-BES Version 1, Program for Coupled Heat, Air, Moisture and Pollutant Simulation in Building Envelope Systems. https://beesl.syr.edu/research/champs-in-building-envelope-systems-champs-bes/. (Accessed 27 July 2023).
Cammalleri, C., La Loggia, G., Maltese, A., 2009. Critical analysis of empirical ground heat flux equation on a cereal field using micrometeorological data. In: Neale, C.M. U., Maltese, A. (Eds.), Remote Sensing for Agriculture, Ecosystems, and Hydrology XI, Proceedings of SPIE - the International Society for Optical Engineering, vol. 7472, 747225. https://doi.org/10.1117/12.830289.
Charisi, S., Thiis, T.K., Stefansson, P., Burud, I., 2018. Prediction model of microclimatic surface conditions on building façades. Built. Environ. 128, 46–54 j.buildenv.2017.11.017.
Chazarra, A., Flórez, E., Peraza, B., Tohá, T., Lorenzo, B., Criado, E., Moreno, J.V., Romero, R., Botey, R., 2018. Climate Maps of Spain (1981-2010) and ETo (1996-2016). Spanish Ministry for Ecological Transition - State Meteorological Agency, Madrid. https://doi.org/10.31978/014-18-004-2 (in Spanish).
Convertino, F., Vox, G., Schettini, E., 2020. In: Proceedings of the Thermal Performance of Exterior Envelopes of Whole Buildings XI International Conference, ASHRAE, 2010.Thermal Barrier Effect on Green Façades: Long-Wave Infrared Radiative Energy Transfer Modelling, vol. 177. Build. Environ., 106875 j.buildenv.2020.106875.
Cornick, S.M., Lacasse, M.A., 2005. A review of climate loads relevant to assessing the watertightness performance of walls, windows and wall-window interfaces. J. ASTM Int. (JAI) 2–10, 1–15. https://doi.org/10.1520/JAI12505.
Delgado, J.M.P.Q., Freitas, V.P., Ramos, N., Barreira, E., 2010. Numerical simulation of exterior condensations on façades: the undercooling phenomenon. In: Proceedings of the Thermal Performance of Exterior Envelopes of Whole Buildings XI International Conference. ASHRAE.
Duffie, J.A., Beckman, W.A., 2013. Solar Engineering of Thermal Processes, fourth ed. John Wiley & Sons, Inc., Hoboken, New Jersey.
EN ISO 15927-3, 2009. Hygrothermal Performance of Buildings. Calculation and Presentation of Climatic Data. Part 3: Calculation of a Driving Rain Index for Vertical Surfaces from Hourly Wind and Rain Data. European Committee for Standardization, Brussels.
EN ISO 52016-1, 2017. Energy Performance of Buildings - Energy Needs for Heating and Cooling, Internal Temperatures and Sensible and Latent Heat Loads - Part 1: Calculation Procedures. European Committee for Standardization, Brussels.
EN ISO 6946, 2021. Building Components and Building Elements - Thermal Resistance and Thermal Transmittance - Calculation Methods. European Committee for Standardization, Brussels.
Erbs, D.G., Klein, S.A., Duffie, J.A., 1982. Estimation of the diffuse radiation fraction for hourly, daily and monthly-average global radiation. Sol. Energy 28:4, 293–302. https://doi.org/10.1016/0038-092X(82)90302-4.
Evett, S.R., Prueger, J.H., Took, J.A., 2011. Water and energy balances in the soil–plant–atmosphere continuum. In: Huang, P.M., Li, Y., Sumner, M.E. (Eds.), Handbook of Soil Sciences: Properties and Processes, second ed. CRC Press, Boca Raton, Florida, pp. 6.1–6.44.
Fraunhofer Institute for Building Physics, 2023. WUFI Software Family for State-Of-The-Art Hygrothermic Analysis. https://wufi.de/en/. (Accessed 27 July 2023).
Gumbel, E.J., 1958. Statistics of Extremes. Columbia University Press, New York.
Hall, C., Hoff, W.D., 2012. Water Transport in Brick, Stone and Concrete, second ed. Spon Press, New York.
Hay, J.E., 1979. Calculation of monthly mean solar radiation for horizontal and inclined surfaces. Sol. Energy 23–4, 301–307. https://doi.org/10.1016/0038-092X(79)90123-3.
Hersbach, H., Bell, B., Berrisford, P., Biavati, G., Horányi, A., Muñoz-Sabater, J., Nicolas, J., Peubey, C., Radu, R., Rozum, I., Schepers, D., Simmons, A., Soci, C., Dee, D., Thépaut, J.N., 2023. ERA5 hourly data on single levels from 1940 to present. Copernicus Climate Change Service (C3S) - Climate Data Store (CDS). https://doi.org/10.24381/cds.adbb2d47.
Jensen, M.E., Burman, R.D., Allen, R.G., 1990. Evapotranspiration and Irrigation Water Requirements, Manual of Practice No. 70, first ed. American Society of Civil Engineers, New York.
Kahangi, S., Niklewski, J., Molnár, M., 2021. Experimental investigation of water absorption and penetration in clay brick masonry under simulated uniform water spray exposure. J. Build. Eng. 43, 102583 https://doi.org/10.1016/j.jobe.2021.102583.
Karn, A., Chintala, V., Kumar, S., 2019. An investigation into sky temperature estimation, its variation, and significance in heat transfer calculations of solar cookers. Heat Transfer-Asian Res. 48 (5), 1830–1856. https://doi.org/10.1002/htj.21459.
Klein, S.A., Theilacker, J.C., 1981. An algorithm for calculating monthly-average radiation on inclined surfaces. J. Sol. Energy Eng. 103, 29–33. https://doi.org/10.1115/1.3266201.
Krayenhoff, E.S., Voogt, J.A., 2010. Impacts of urban albedo increase on local air temperature at daily–annual time scales: model results and synthesis of previous work. J. Appl. Meteorol. Climatol. 49, 1634–1648. https://doi.org/10.1175/2010JAMC2356.1.
Kubilay, A., Bourcet, J., Gravel, J., Zhou, X., Moore, T.V., Lacasse, M.A., Carmeliet, J., Derome, D., 2021. Combined use of wind-driven rain load and potential evaporation to evaluate moisture damage risk: case study on the Parliament buildings in Ottawa, Canada. Buildings 11–10, 476. https://doi.org/10.3390/buildings11100476.
Künzel, H.M., Schmidt, T., Holm, A., 2002. Exterior surface temperature of different wall constructions: comparison of numerical simulation and experiment. In: Proceedings of the 11th Symposium for Building Physics. TU Dresden, pp. 441–449.
Liendhard IV, J.H., Liendard V, J.H., 2020. A Heat Transfer Textbook, fifth ed. Phlogiston Press, Cambridge, Ma.
Maleki, S.A.M., Hizam, H., Gomes, C., 2017. Estimation of hourly, daily and monthly global solar radiation on inclined surfaces: models re-visited. Energies 10, 134. https://doi.org/10.3390/en10010134.
Marino, B.M., Muñoz, N., Thomas, L.P., 2018. Calculation of the external Surface temperature of a multi-layer Wall considering solar radiation effects. Energy Build. 174, 452–463 j.enbuild.2018.07.008.
Mira, M., Gordillo, J., González, O., Pons, X., 2017. Comparative analysis of methods for estimating emissivity in the thermal band of the Landsat-5 TM sensor. Geofocus International Review of Geographical Information Science and Technology 19, 55–80. https://doi.org/10.21138/GF.512 (In Spanish).
Oke, T.R., 1987. Boundary Layer Climates, second ed. Methuen & Co. Ltd., London, England.
Olsson, L., 2018. Driving rain tightness, intrusion rates and phenomenology of leakages in defects of façades: a new calculation algorithm. In: PhD Thesis. Chalmers University of Technology, Gothenburg.
Orr, S.A., Viles, H., 2018. Characterisation of building exposure to wind-driven rain in the UK and evaluation of current standards. J. Wind Eng. Ind. Aerod. 180, 88–97. https://doi.org/10.1016/j.jweia.2018.07.013.
Orr, S.A., Young, M., Stelfox, D., Curran, J., Viles, H., 2018. Wind-driven rain and future risk to built heritage in the United Kingdom: novel metrics for characterising rain spells. Sci. Total Environ. 640–641C, 1098–1111. https://doi.org/10.1016/j.scitotenv.2018.05.354.
Peel, M.C., Finlayson, B.L., Mcmahon, T.A., 2007. Updated world map of the Köppen-Geiger climate classification. Hydrol. Earth Syst. Sci. 11, 1633–1644. https://doi.org/10.5194/hess-11-1633-2007.
Penman, H.L., 1948. Natural evaporation from open water, bare soil, and grass. Proc. Roy. Soc. Lond. 193 (1032), 120–145. https://doi.org/10.1098/rspa.1948.0037.
Pérez, J.M., Domínguez, J., Cano, E., del Coz, J.J., Álvarez, F.P., 2018. On the significance of the climate-dataset time resolution in characterising wind-driven rain and simultaneous wind pressure. Part II: directional analysis. Stoch. Environ. Res. Risk Assess. 32, 1799–1815. https://doi.org/10.1007/s00477-017-1480-2.
Pérez, J.M., Domínguez, J., Cano, E., Alonso, M., del Coz, J.J., 2020a. Equivalence between the methods established by ISO 15927-3 to determine wind-driven rain exposure: reanalysis and improvement proposal, Build. Environ. Times 174, 106777. https://doi.org/10.1016/j.buildenv.2020.106777.
Pérez, J.M., Domínguez, J., Cano, E., Alonso, M., del Coz, J.J., 2020b. Equivalence between the methods established by ISO 15927-3 to determine wind-driven rain exposure: reanalysis and improvement proposal, Build. Environ. Times 174, 106777. https://doi.org/10.1016/j.buildenv.2020.106777.
Prior, M.J., 1985. Directional Driving Rain Indices for the United Kingdom: Computation and Mapping (Background to BSI Draft for Development DD93). Building Research Establishment, Garston.
Ronoh, E.K., 2021. Radiation exchange at greenhouse tilted surfaces under all-sky conditions. In: Shamshiri, R.R. (Ed.), Next-generation Greenhouses for Food Security, first ed., Intechopen, p. 14.13 4.
Royal Netherlands Meteorological Institute (KNMI), 2022. Weather Stations – Hourly Records (in Dutch). https://www.daggegevens.knmi.nl/klimatologie/uurgegevens. (Accessed 27 July 2023).
Sauni, R., Verbeek, J.H., Uitti, J., Jauhiainen, M., Kreiss, K., Sigsgaard, T., 2015. Remediating buildings damaged by dampness and mould for preventing or reducing respiratory tract symptoms, infections and asthma. Cochrane Database Syst. Rev. 2, CD007897 https://doi.org/10.1002/14651858.CD007897.pub3.
Shahreza, S.K., Niklewski, J., Molnár, M., 2022. Novel water penetration criterion for clay brick masonry claddings. Construct. Build. Mater. 353, 129109 https://doi.org/10.1016/j.conbuildmat.2022.129109.
Shirsath, P.B., Singh, A.K., 2010. A comparative study of daily pan evaporation estimation using ANN, regression and climate based models. Water Resour. Manag. 24, 1571–1581. https://doi.org/10.1007/s11269-009-9514-2.
Shuttleworth, W.J., 2007. Putting the 'vap' into evaporation. Hydrol. Earth Syst. Sci. 11 (1), 210–244. https://doi.org/10.5194/hess-11-210-2007.
Shuttleworth, W.J., 1993. Evaporation (chapter 4). In: Maidment, D.R. (Ed.), Handbook of Hydrology. McGraw-Hill Inc, New York, pp. 4.1–4.53.
Smith, R.L., 1990. Extreme value theory. In: Ledermann, W. (Ed.), Handbook of Applicable Mathematics. John Wiley, Chichester, pp. 437–471.
Spanish Ministry of Development, 2022. Supporting Documents for the DB-HE Basic Document of Energy Saving -Technical Building Code- (in Spanish). https://www.codigotecnico.org/DocumentosCTE/AhorroEnergia.html. (Accessed 27 July 2023).

The Netherlands central government, Building decree 2012 - practical book (in Dutch). https://www.rijksoverheid.nl/documenten/richtlijnen/2011/10/05/praktijkboek-bouwbesluit-2012, (accessed 27 July 2023).

Trlica, A., Hutyra, L.R., Schaad, C.L., Erb, A., Wang, J.A., 2017. Albedo, land cover, and daytime surface temperature variation across an urbanized landscape. Earth's Future 5, 1084–1101. https://doi.org/10.1002/2017EF000569.

Van Den Bossche, N., Lacasse, M., Janssens, A., 2011. Watertightness of masonry walls: an overview. In: de Freitas, V.P., Corvacho, H., Lacasse, M.A. (Eds.), Proceedings of 12th International Conference on the Durability of Building Materials and Components (12DBMC). U. Porto Edições, pp. 1–8.

Van Linden, S., Van Den Bossche, N., 2022. Review of rainwater infiltration rates in wall assemblies. Build. Environ. 219, 109213 https://doi.org/10.1016/j.buildenv.2022.109213.

Walter, I.A., Allen, R.G., Elliott, R., Itenfisu, D., Brown, P., Jensen, M.E., Mecham, B., Howell, T.A., Snyder, R., Eching, S., Spofford, T., Hattendorf, M., Martin, D., Cuenca, R.H., Wright, J.L., 2005. The ASCE standardized reference evapotranspiration equation. ASCE-EWRI Task Committee Report. https://doi.org/10.1061/9780784408056.

Wittich, K.P., 1997. Some simple relationships between land-surface emissivity, greenness and the plant cover fraction for use in satellite remote sensing. Int. J. Biometeorol. 41, 58–64. https://doi.org/10.1007/s004840050054.

WMO, 2008. Guide to Meteorological Instruments and Methods of Observation (WMO-No 8). World Meteorological Organization, Geneva.

Zhang, K., McDowell, T.P., Kummert, M., 2017. Sky temperature estimation and measurement for longwave radiation calculation. In: Barnaby, C.S., Wetter, M. (Eds.), Proceedings of the 15th IBPSA Conference (Building Simulation 2017), International Building Performance Simulation Association, pp. 2093–2102. https://doi.org/10.26868/25222708.2017.569.

Zhou, X., Derome, D., Carmeliet, J., 2016. Robust moisture reference year methodology for hygrothermal simulations. Build. Environ. 110, 23–35. https://doi.org/10.1016/j.buildenv.2016.09.021.